

# Letter of Intent for KASKA

High Accuracy Neutrino Oscillation Measurements  
with  $\bar{\nu}_e$ s from  
*Kashiwazaki-Kariwa Nuclear Power Station.*

M. Aoki<sup>5</sup>, *K.Akiyama*<sup>4,a</sup>, Y. Fukuda<sup>4</sup>, *A.Fukui*<sup>3,b</sup>,  
Y. Funaki<sup>9</sup>, H. Furuta<sup>9</sup>, T. Hara<sup>3</sup>, T. Haruna<sup>10</sup>,  
N. Ishihara<sup>2</sup>, *T.Iwabuchi*<sup>5,c</sup>, M. Katsumata<sup>5</sup>,  
T. Kawasaki<sup>5</sup>, M. Kuze<sup>9</sup>, J. Maeda<sup>9</sup>,  
T. Matsubara<sup>9</sup>, *T.Matsumoto*<sup>10,d</sup>, H. Minakata<sup>10</sup>,  
H. Miyata<sup>5</sup>, Y. Nagasaka<sup>1</sup>, *T.Nakagawa*<sup>10,e</sup>,  
N. Nakajima<sup>5</sup>, H. Nakano<sup>5</sup>, K. Nitta<sup>9</sup>,  
M. Nomachi<sup>6</sup>, K. Sakai<sup>5</sup>, Y. Sakamoto<sup>8</sup>,  
*K.Sakuma*<sup>10,f</sup>, M. Sasaki<sup>5</sup>, F. Suekane<sup>7</sup>,  
H. Sugiyama<sup>2</sup>, T. Sumiyoshi<sup>10</sup>, H. Tabata<sup>7</sup>,  
N. Tamura<sup>5</sup>, M. Tanimoto<sup>5</sup>, Y. Tsuchiya<sup>7</sup>,  
*R.Watanabe*<sup>5</sup> and O. Yasuda<sup>10</sup>

August 15, 2018

The people with italic name are not current KASKA members, but have contributed to this LoI.

1. Hiroshima Institute of Technology
2. High Energy Accelerator Research Organization (KEK)
3. Kobe University
4. Miyagi University of Education
5. Niigata University
6. Osaka University
7. Tohoku University
8. Tohoku Gakuin University
9. Tokyo Institute of Technology
10. Tokyo Metropolitan University

Present Address:

<sup>a</sup> Tohoku University

<sup>b</sup> Nagoya University

<sup>c</sup> Fujitsu Integrated Micro Technology

<sup>d</sup> KEK

<sup>e</sup> Hewlett-Packerd Japan, Ltd

<sup>f</sup> Ministry of Economy, Trade and Industry

# Contents

<b>1</b>	<b>Introduction</b>	<b>2</b>
1.1	Physics Background and $\theta_{13}$ . . . . .	2
1.2	Reactor Neutrino Oscillation . . . . .	4
1.3	Why reactor measurement? . . . . .	9
<b>2</b>	<b>General Description of the Experiment</b>	<b>13</b>
2.1	Kashiwazaki-Kariwa Nuclear Power Station . . . . .	13
2.2	Reactor Neutrinos . . . . .	16
2.3	General Description of Neutrino Detector . . . . .	19
2.4	Sensitivities of KASKA . . . . .	23
2.4.1	$\sin^2 2\theta_{13}$ measurement . . . . .	23
2.4.2	High statistics reactor $\bar{\nu}_e$ measurement . . . . .	23
2.5	Possible Future Extensions of the KASKA project . . . . .	26
2.5.1	KASKA-II: Detecting non-0 $\delta_l$ . . . . .	26
2.5.2	KASKA- $\theta_{12}$ : Accurate $\sin^2 2\theta_{12}$ measurement . . . . .	26
2.5.3	KASKA- $\Delta m_{13}^2$ : Independent $\Delta m_{13}^2$ measurement . . . . .	29
<b>3</b>	<b>Detector</b>	<b>30</b>
3.1	Mechanical Structure . . . . .	30
3.2	Liquid Scintillators . . . . .	33
3.2.1	Neutrino Target (Region-I) . . . . .	35
3.2.2	$\gamma$ -ray catcher (Region-II) . . . . .	35
3.2.3	Buffer oil (Region-III&IV) . . . . .	36
3.2.4	Cosmic-ray veto (Region-V) . . . . .	36
3.3	Photosensor . . . . .	36
3.4	Cosmic-ray Tracking Device . . . . .	37
3.4.1	A case of LS-based detector . . . . .	41
3.4.2	A case of PS-based detector . . . . .	41
<b>4</b>	<b>Shaft Hole</b>	<b>42</b>
<b>5</b>	<b>Readout Electronics</b>	<b>44</b>
5.1	Property of Signals . . . . .	44
5.2	Electronics Scheme . . . . .	49
5.3	Trigger . . . . .	52
5.4	Readout modules . . . . .	52
<b>6</b>	<b>Calibration</b>	<b>54</b>
6.1	Introduction . . . . .	54
6.2	Optical and electronic calibrations . . . . .	54
6.3	Energy calibration . . . . .	55
6.3.1	$\gamma$ ray sources . . . . .	55
6.3.2	Positron sources . . . . .	55
6.3.3	Neutron sources . . . . .	56

6.4	Calibration device manipulator . . . . .	56
6.4.1	Wire type manipulator . . . . .	56
6.4.2	Robot arm type manipulator . . . . .	57
<b>7</b>	<b>Backgrounds</b>	<b>58</b>
7.1	Background Sources . . . . .	60
7.1.1	Internal Background . . . . .	62
7.1.2	External Background . . . . .	63
7.1.3	Cosmic Rays . . . . .	64
7.2	Accidental Backgrounds . . . . .	68
7.3	Correlated Backgrounds . . . . .	68
7.3.1	Fast Neutron Background . . . . .	69
7.3.2	Spallation Background . . . . .	70
7.3.3	Stopping $\mu$ . . . . .	70
<b>8</b>	<b>Systematic Error</b>	<b>71</b>
8.1	Near/Far cancellation . . . . .	72
8.2	Detector Associated Error; $\delta_{uncorr}(\epsilon N_p)/\epsilon N_p$ . . . . .	74
8.2.1	Number of target protons; $N_p$ . . . . .	74
8.2.2	$e^+$ Energy Cut Efficiency; $\epsilon_{e^+}$ . . . . .	75
8.2.3	Neutron Capture Efficiency; $\epsilon_n$ . . . . .	76
8.2.4	n Energy Cut Efficiency; $\epsilon_n$ . . . . .	76
8.2.5	Efficiency for the timing cut; $\epsilon_{\Delta t}$ . . . . .	77
8.3	Error from Reactor Neutrino Flux; $f_\nu$ . . . . .	78
8.4	systematics summary . . . . .	78
<b>9</b>	<b>Conclusions</b>	<b>78</b>
<b>A</b>	<b>Acknowledgement</b>	<b>80</b>

# 1 Introduction

## 1.1 Physics Background and $\theta_{13}$

Since neutrinos have peculiar properties such as very small masses, very much different mixing patterns from quark sector and possibility of being Majorana particle, study of neutrinos is very important to understand the nature of the elementary particles and to construct its unified theory in the future. Because the neutrinos have finite masses and mixing, they perform neutrino oscillation if their masses are not identical. For two flavor case, the probability that a particular flavor neutrino  $\nu_x$  with energy  $E_\nu$  to remain as  $\nu_x$  after traveling a distance  $L$  becomes,

$$P_{\nu_x \rightarrow \nu_x} = 1 - \sin^2 2\theta \sin^2 \Phi, \quad (1)$$

$$\Phi = \frac{\Delta m^2 L}{4E_\nu}$$

due to the neutrino oscillation, where  $\Delta m^2$  is the difference of the squared masses between the two mass eigen states;  $m_2^2 - m_1^2$ , and  $\theta$  is the mixing angle between mass eigenstate and flavor eigenstate. Through neutrino oscillation, it is possible to access to a very small mass range where direct measurements are difficult to reach and to measure the mixing angle.

For 3 flavor case, the flavor eigenstates;  $\nu_e, \nu_\mu$  and  $\nu_\tau$ , and mass eigenstates;  $\nu_1, \nu_2$  and  $\nu_3$ , are mixed by  $3 \times 3$  Maki-Nakagawa-Sakata (MNS) matrix [1].

$$\begin{pmatrix} \nu_e \\ \nu_\mu \\ \nu_\tau \end{pmatrix} = \begin{pmatrix} U_{e1} & U_{e2} & U_{e3} \\ U_{\mu1} & U_{\mu2} & U_{\mu3} \\ U_{\tau1} & U_{\tau2} & U_{\tau3} \end{pmatrix} \begin{pmatrix} \nu_1 \\ \nu_2 \\ \nu_3 \end{pmatrix} = U_{MNS} \begin{pmatrix} \nu_1 \\ \nu_2 \\ \nu_3 \end{pmatrix} \quad (2)$$

In this case, three flavor oscillation formula becomes,

$$\begin{aligned} & \left\{ \begin{array}{l} P(\nu_\alpha \rightarrow \nu_\beta) \\ P(\bar{\nu}_\alpha \rightarrow \bar{\nu}_\beta) \end{array} \right\} \\ &= \delta_{\alpha\beta} - 4 \sum_{i>j} \Re(U_{\alpha i}^* U_{\beta i} U_{\alpha j} U_{\beta j}^*) \sin^2 \Phi_{ij} \pm 2 \sum_{i>j} \Im(U_{\alpha i}^* U_{\beta i} U_{\alpha j} U_{\beta j}^*) \sin 2\Phi_{ij} \end{aligned} \quad (3)$$

where  $\alpha, \beta$  are indices of flavors and  $i, j$  are indices of masses with  $m_i$  being the mass of  $\nu_i$ .  $\Phi_{ij} = \frac{\Delta m_{ij}^2 L}{4E_\nu}$  represent oscillation phase caused by the difference of mass square,  $\Delta m_{ij}^2 = m_j^2 - m_i^2$ .

The MNS matrix can be expressed by 4 parameters;

$$\begin{aligned}
U_{MNS} &= \begin{pmatrix} 1 & 0 & 0 \\ 0 & c_{23} & s_{23} \\ 0 & -s_{23} & c_{23} \end{pmatrix} \begin{pmatrix} c_{13} & 0 & s_{13}e^{i\delta_l} \\ 0 & 1 & 0 \\ -s_{13}e^{-i\delta_l} & 0 & c_{13} \end{pmatrix} \begin{pmatrix} c_{12} & s_{12} & 0 \\ -s_{12} & c_{12} & 0 \\ 0 & 0 & 1 \end{pmatrix} \\
&= \begin{pmatrix} c_{13}c_{12} & c_{13}s_{12} & s_{13}e^{i\delta_l} \\ -c_{23}s_{12} - s_{13}s_{23}c_{12}e^{-i\delta_l} & c_{23}c_{12} - s_{13}s_{23}s_{12}e^{-i\delta_l} & c_{13}c_{23} \\ s_{23}s_{12} - s_{13}c_{23}c_{12}e^{-i\delta_l} & -c_{13}s_{23} - s_{13}c_{23}s_{12}e^{-i\delta_l} & c_{13}c_{23} \end{pmatrix} \quad (4)
\end{aligned}$$

where  $c_{ij}$  and  $s_{ij}$  express  $\cos\theta_{ij}$  and  $\sin\theta_{ij}$ , respectively.

Experimental studies of the neutrino oscillations have been progressing very rapidly in these days. The first firm evidence of the neutrino oscillation was discovered in the disappearance of muon type atmospheric neutrinos by SuperKamiokande (SK) group in 1998 [2]. SK group has been taking more data and recently observed spectrum distortion [3], which is consistent with oscillation pattern. K2K group confirmed the result [4] by observing the disappearance of  $\nu_\mu$  produced by the KEK-PS accelerator, after traveling 250 km. These phenomena are naturally explained by the  $\nu_\mu \rightarrow \nu_\tau$  oscillation since there is no significant enhancement in  $\nu_e$  spectrum. The measured oscillation parameters are  $\Delta m_{23}^2 \approx 2.4 \times 10^{-3} eV^2$  and  $\sin^2 2\theta_{23} \approx 1$ . As for the electron type neutrinos there have been indications of the neutrino oscillation in the deficit of the solar neutrinos for a long time [5]. A transformation of the solar  $\nu_e$  to other type neutrinos was identified by combining SNO data and SK data in 2002 [6, 7]. Finally, the KamLAND group observed a large deficit in reactor  $\bar{\nu}_e$  in 2002 [8] and then spectral distortion in 2005 [9]. Combined with solar neutrino data, the oscillation parameters are measured as  $\Delta m_{12}^2 \approx 7.9 \times 10^{-5} eV^2$  and  $\tan^2 \theta_{12} \approx 0.40$ . With these measurements, measurable 2 mass combinations and 2 mixing angles out of 3 are already measured. The sign of  $\Delta m_{12}^2$  is determined to be  $> 0$  by MSW matter effect of solar neutrinos. However, the sign of  $\Delta m_{23}^2$  is not determined yet. Finite  $\theta_{13}$  and  $\delta_l$  have not been measured yet. The most stringent upper limit of  $\theta_{13}$  was measured by CHOOZ group using reactor  $\bar{\nu}_e$ s to be  $\sin^2 2\theta_{13} < 0.15$  at  $\Delta m^2 = 2.5 \times 10^{-3} eV^2$  [10]. As for  $\delta_l$  parameter, there is no information by now. By combining measured parameters, the magnitudes of MNS matrix elements are determined to be roughly,

$$|U_{MNS}| \approx \begin{pmatrix} 0.8 & 0.5 & < 0.2 \\ 0.4 & 0.6 & 0.7 \\ 0.4 & 0.6 & 0.7 \end{pmatrix} \quad (5)$$

and the relation of masses and flavor components of mass eigenstates are shown in Fig. 1. The elements of the MNS matrix are very much different from those of the Cabbibo-Kobayashi-Maskawa Matrix, which is nearly diagonal. The  $U_{e3}$  element (and thus  $\sin\theta_{13}$ ) is small compared to other elements. This peculiar feature has to be explained by the unified theory of elementary particles and the smallness of the  $\theta_{13}$  may play a key role when constructing the unified theory.

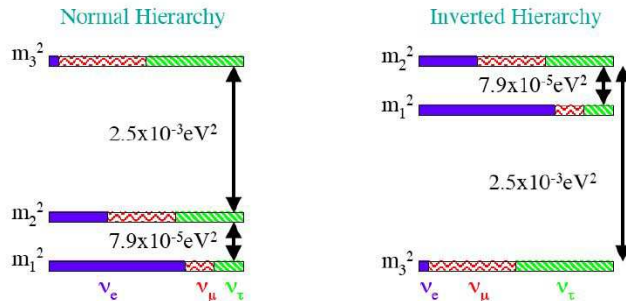


Figure 1: The relation of neutrino masses and flavor components of mass eigenstates. There are two possibilities in the mass relations according to the sign of  $\Delta m_{23}^2$ . The case of  $\Delta m_{23}^2 > 0$  ( $\Delta m_{23}^2 < 0$ ) is called 'normal hierarchy' ('inverted hierarchy'). The  $\nu_e$  component of  $\nu_3$  is less than 4%. Other mixings are relatively large.

As for the  $\delta_l$ , the  $e^{i\delta_l}$  term is multiplied by  $\sin\theta_{13}$  in the Eq.(4). Thus the effect of CP violation phenomena is proportional to  $\sin\theta_{13}$ . For example, the detectability of finite  $\delta_l$  from asymmetry of  $P(\nu_\mu \rightarrow \nu_e)$  and  $P(\bar{\nu}_\mu \rightarrow \bar{\nu}_e)$  in near-future accelerator based neutrino experiments depends on the size of  $\theta_{13}$  as shown in Fig. 2. Therefore it is important to know the magnitude of  $\sin\theta_{13}$  to evaluate the effect of leptonic CP violation, which may explain the matter-antimatter asymmetry of the current universe.

KamLAND experiment measured a deficit of reactor neutrino at average baseline 180km. For three generations, what KamLAND observed is expressed as,

$$P(\bar{\nu}_e \rightarrow \bar{\nu}_e) = \cos^4 \theta_{13} (1 - \sin^2 2\theta_{12} \sin^2 \Phi_{12}) \quad (6)$$

There is  $\sim 5\%$  of ambiguity introduced by the  $\theta_{13}$  term, when determining  $\sin^2 \theta_{12}$  from KamLAND oscillation. Therefore precise measurement  $\theta_{13}$  helps to obtain more accurate  $\theta_{12}$  from the KamLAND data.

Thus there are number of reasons why measurement of  $\theta_{13}$  is one of the most urgent topics of the neutrino physics.

## 1.2 Reactor Neutrino Oscillation

In reactors, huge amount of low energy  $\bar{\nu}_e$ 's are produced in the  $\beta$ -decays of the fission product nuclei. A typical reactor with thermal power of 3GW isotropically produces the Avogadro number of  $\bar{\nu}_e$ 's in 15 minutes. The average  $\bar{\nu}_e$  energy detected through  $\bar{\nu}_e + p \rightarrow e^+ + n$  interaction is around 4 MeV. These properties of huge number and low energy of reactor  $\bar{\nu}_e$  are suitable to use to measure neutrino oscillation.

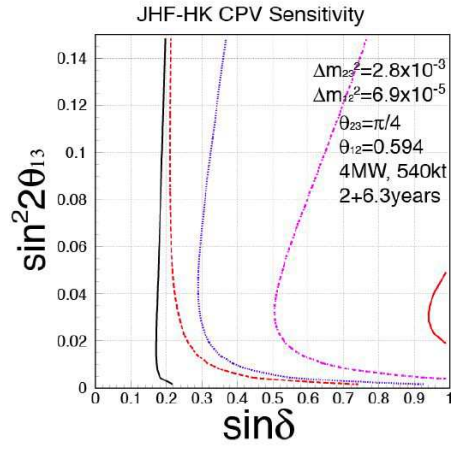


Figure 2: Expected  $3\sigma$  discovery regions of  $\sin \delta_l$  as a function of  $\sin^2 2\theta_{13}$  after  $2(\nu_\mu)$  and  $6.3(\bar{\nu}_\mu)$  year of exposure in phase II of the JHF-Kamioka project (J-PARC). The (black) solid curve is the case of no background and only statistical error of the signal, (red) dashed one is 2% error for the background subtraction, and (blue) dotted, (magenta) dot-dashed and (red) solid curves are the cases for systematic errors of both background subtraction and signal detection of 2%, 5% and 10%, respectively [16].



In 3 generations, the  $\bar{\nu}_e \rightarrow \bar{\nu}_e$  oscillation formula is calculated from the Eq.(3) and (4) as ,

$$P(\bar{\nu}_e \rightarrow \bar{\nu}_e) = 1 - 4c_{13}^2(c_{13}^2 s_{12}^2 c_{12}^2 \sin^2 \Phi_{21} + s_{13}^2 c_{12}^2 \sin^2 \Phi_{31} + s_{13}^2 s_{12}^2 \sin^2 \Phi_{32}). \quad (7)$$

Because  $|\Phi_{31}| = |\Phi_{12} + \Phi_{23}| \approx |\Phi_{23}|$ , there are essentially two types of oscillations; one is driven by  $\Delta m_{13}^2$  at around 2km and the other one is driven by  $\Delta m_{12}^2$  at around 50km.

Fig. 3 shows the survival probability of 4 MeV  $\bar{\nu}_e$  in case  $\sin^2 2\theta_{13} = 0.1$ .

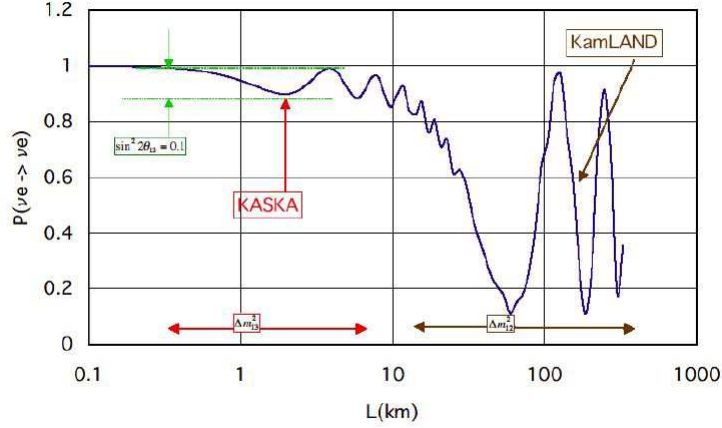


Figure 3:  $\bar{\nu}_e$  oscillation with 3 generations.

KamLAND, which measured  $\sin^2 2\theta_{12}$  and  $\Delta m_{12}^2$  at around  $L \sim 180km$ , has demonstrated power of reactor measurement of neutrino oscillation. Fig. 4 shows the oscillation pattern of the reactor neutrino measured by the KamLAND experiment. KamLAND detected an energy-dependent deficit of the reactor neutrino. A clear oscillatory pattern is observed in Fig. 4.

Fig. 5 shows the oscillation parameters measured by KamLAND only (left plot) and KamLAND+ Solar analysis (right plot). From these measurement,  $\tan^2 \theta \sim 0.4$ ,  $\Delta m^2 \sim 8 \times 10^{-5} eV^2$  are obtained.

KASKA aims to measure the  $\sin^2 2\theta_{13}$  at around  $L \sim 1.6$  km; 1/100th baseline of KamLAND. At the distance, the Eq.(7) reduces to,

$$P(\bar{\nu}_e \rightarrow \bar{\nu}_e) = 1 - \sin^2 2\theta_{13} \sin^2 \Phi_{13} + O(10^{-3}) \quad (8)$$

Therefore almost pure  $\sin^2 2\theta_{13}$  can be measured. The current best limit on  $\sin^2 2\theta_{13}$  is obtained by CHOOZ reactor experiment in France. The CHOOZ experiment used two powerful reactors whose total thermal energy is  $8.5 \text{ GW}_{th}$ .

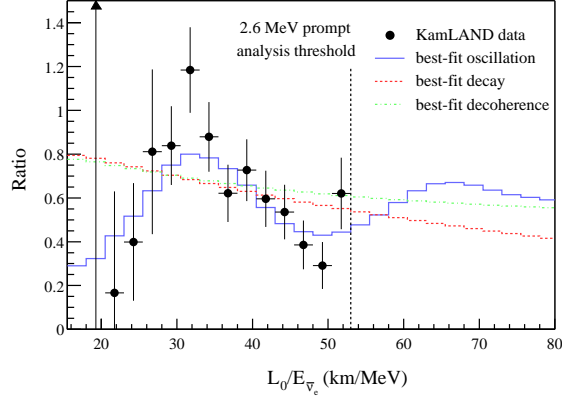


Figure 4: Oscillation pattern of the reactor neutrinos measured by KamLAND at an average baseline 180km. [9]

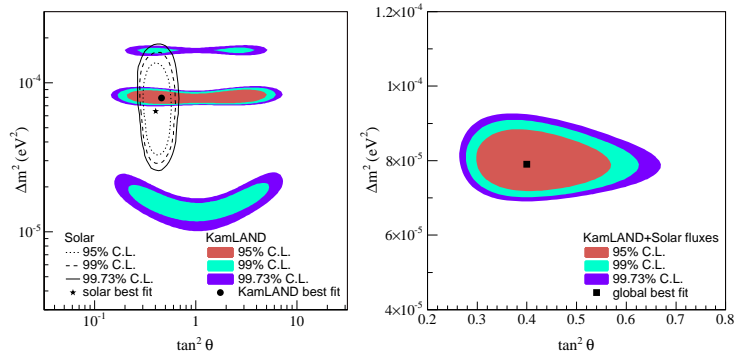


Figure 5: Oscillation parameters of electron type neutrinos. The KamLAND results (Left) and after combination with solar neutrino experiments. [9]

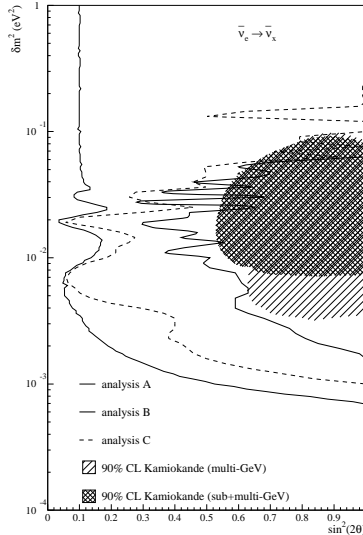


Figure 6: CHOOZ  $\sin^2 2\theta_{13}$  limits [10].

The detector is placed at 1km from the reactors and the result of the measurements are shown in Fig. 6. They did not confirm the positive result and showed the upper limit of  $\sin^2 2\theta_{13} < 0.15$  for  $\Delta m_{13}^2 = 2.5 \times 10^{-3} eV^2$ .

The PaloVerde experiment also searched for the deficit of reactor neutrino with average baseline 0.8km using PaloVerde reactor complex in Arizona, USA, whose total thermal energy is 11.63  $GW_{th}$ . They did not observe the deficit of the reactor neutrino and the limit of the oscillation measurement is shown in Fig. 7.

In view of the currently known  $\Delta m_{23}^2$ , the baselines of those experiments were somewhat shorter than most probable oscillation maximum of 1.8 km. The measurement errors were rather large due to uncertainties of reactor neutrino flux as well as detector associated absolute errors and low statistics.

The KASKA experiment is going to measure this oscillation using the  $\bar{\nu}_e$ 's from world most powerful Kashiwazaki-Kariwa nuclear power station with optimized baseline. Four identical detectors, of which two are placed near the reactors and other two are placed at around 1.6 km from the reactors, are used. By comparing the data taken at near and far distances, most of the systematic uncertainties are cancelled out and precise measurement becomes possible. This far-near cancellation scheme for the  $\theta_{13}$  measurement was first proposed by Krasnoyarsk group [12]. Fig. 22 shows the expected sensitivity for  $\sigma_{rel} = 1\%$  and 0.5% with 3 years of data. It is possible to obtain 10 times better sensitivity than current CHOOZ limit.

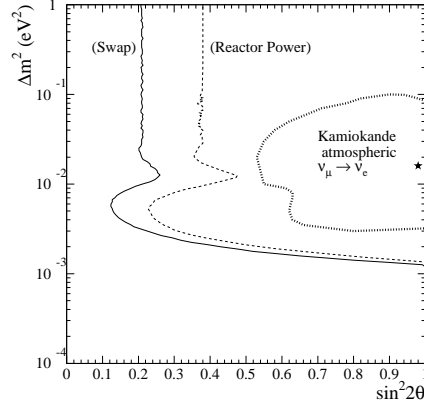


Figure 7: Result of PaloVerde experiment. [11]

### 1.3 Why reactor measurement?

Near-future long baseline accelerator experiments (LBL) also have sensitivity to  $\sin^2 2\theta_{13}$  [15, 13]. In such experiments, high energy  $\nu_\mu$ 's are produced by accelerator and appearance of  $\nu_e$ 's is searched for after traveling a few hundred km. The probability of  $\nu_\mu \rightarrow \nu_e$  transition at the oscillation maximum is expressed by the following equation.

$$\begin{aligned}
 P(\nu_\mu \rightarrow \nu_e) &\approx f^2 \sin^2 2\theta_{13} \sin^2 \theta_{23} \\
 &- \left| \frac{\Delta m_{12}^2}{\Delta m_{23}^2} \right| f g \cos \theta_{13} \sin 2\theta_{12} \sin 2\theta_{23} \sin 2\theta_{13} \sin \delta_l \\
 &+ \left| \frac{\Delta m_{12}^2}{\Delta m_{23}^2} \right|^2 g^2 \cos^2 \theta_{23} \sin^2 2\theta_{12},
 \end{aligned} \tag{9}$$

where

$$\begin{aligned}
 f &\equiv \frac{\cos(AL/2)}{1 \mp AL/\pi} \\
 g &\equiv \frac{\sin(AL/2)}{AL/\pi} \\
 A &\equiv \sqrt{2} G_F N_e,
 \end{aligned}$$

and  $AL/\pi \simeq 5 \times 10^{-2}$  for  $L=300$  km. The sign in the definition of  $f$  is  $-$  ( $+$ ) for the normal (inverted) hierarchy. This measurement depends on many parameters which are not necessarily well known. Since  $\sin^2 2\theta_{12}$  and  $\Delta m_{12}^2$  have turned out not so small by KamLAND and solar neutrino experiments, the 2nd term in Eq.(9) cannot be ignored any more (this very reason enables the measurement of  $\delta_l$  in future LBL experiments). Because  $\sin \delta_l$  is totally

unknown, the 2nd term becomes ambiguity when determining  $\sin^2 2\theta_{13}$  from the  $\nu_e$  appearance probability. Furthermore, there is an ambiguity of  $\theta_{23}$  degeneracy, which means there are two possible  $\sin^2 \theta_{23}$  corresponding to measured  $\sin^2 2\theta_{23}$  value, if it is not unity as,

$$\sin^2 \theta_{23} = \frac{1 + \sqrt{1 - \sin^2 2\theta_{23}}}{2} \text{ or } \frac{1 - \sqrt{1 - \sin^2 2\theta_{23}}}{2} \quad (10)$$

This degeneracy of  $\theta_{23}$  disturbs the  $\theta_{13}$  determination by LBL experiments further. These situations for the case of  $\sin^2 2\theta_{23} = 0.95$  and  $0.98$  are depicted in Fig. 8 and 9.

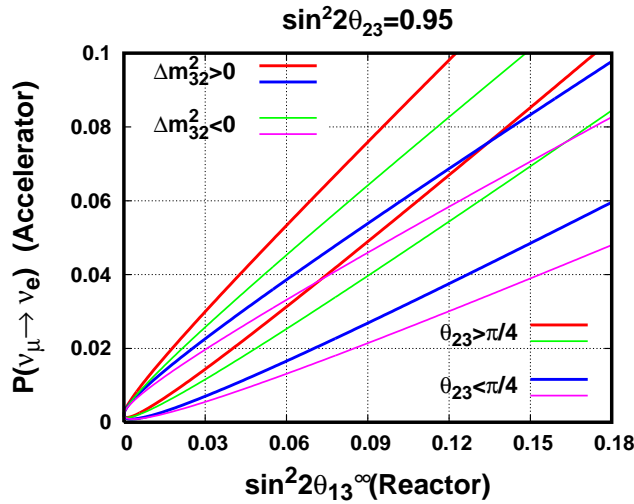


Figure 8: sensitivity of Long Base Line neutrino experiments ( $\sin^2 2\theta_{23}=0.95$ )

The area bounded by each parabola implies the  $\sin \delta_l$ -term ambiguity and the  $\theta_{23}$  degeneracy corresponds to two parabolas. Thus even if LBL experiment measures  $P(\nu_\mu \rightarrow \nu_e)$  precisely, there is ambiguity in determining the  $\sin^2 2\theta_{13}$ . On the other hand, the reactor based  $\bar{\nu}_e$  oscillation measurement is a pure  $\sin^2 2\theta_{13}$  measurement as shown in Eq.(8). The expected error on  $\sin^2 2\theta_{13}$  is  $\pm 0.01$  and for some parameter regions, the error of reactor measurement is better than the ambiguities in  $\sin^2 2\theta_{13}$  determination by LBL experiments. Basically LBL and reactor experiment measure different parameters and if both results are combined, there are possibilities to solve the  $\theta_{23}$  degeneracy as shown in the Fig. 10. The possibility to remove the  $\theta_{23}$  ambiguity by a reactor experiment was pointed out first in [17], and was elaborated in detail by KASKA group members [18] using a realistic scenario. Thus it is important to know the magnitude of  $\sin \theta_{13}$  to evaluate the effect of leptonic CP violation, which may explain the matter-antimatter asymmetry of the current universe.

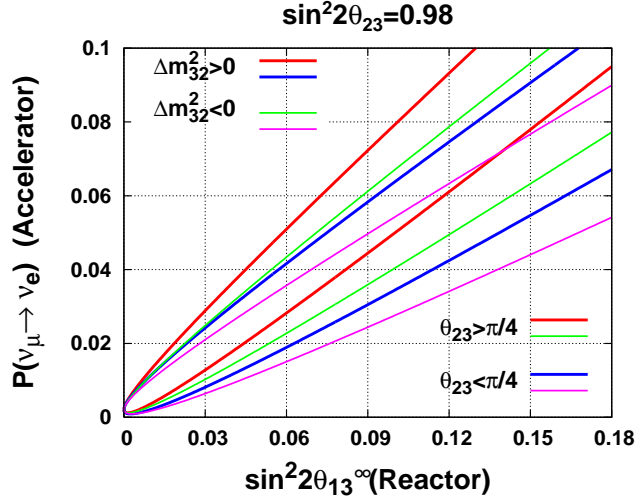


Figure 9: sensitivity of Long Base Line neutrino experiments ( $\sin^2 2\theta_{23}=0.98$ )

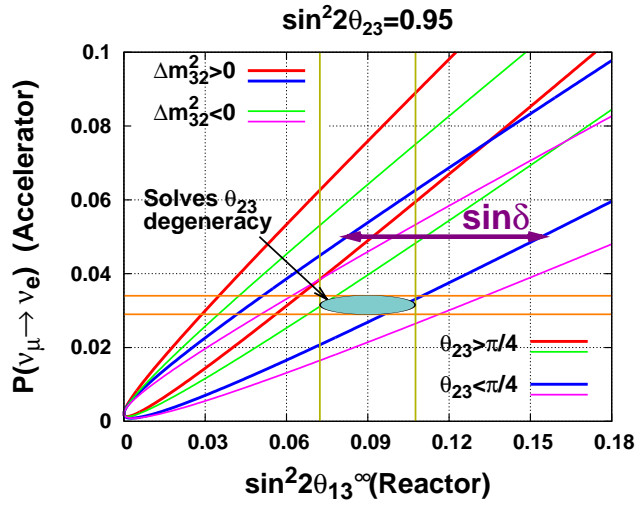


Figure 10:  $\theta_{23}$  degeneracy can be solved by combining reactor and accelerator experiment.

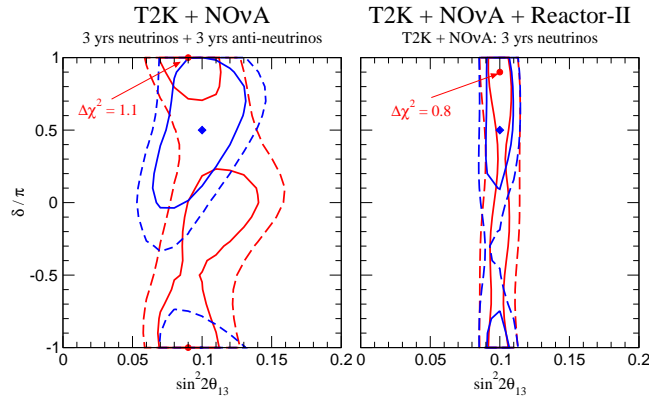


Figure 11: Antineutrino running vs reactor-II ( $\delta \sin^2 2\theta_{13} \sim 0.01$ ). The 90% CL (solid curve) and  $3\sigma$  (dashed curves) allowed regions in the  $\sin^2 2\theta_{13} - \delta_l$ -plane for the true values  $\sin^2 2\theta_{13} = 0.1$  and  $\delta_l = \pi/2$ , are shown. The blue/dark curves refer to the allowed regions for the normal mass hierarchy, whereas the red/light curves refer to the  $\text{sgn}(\Delta_{13}^2)$ -degenerate solution (inverted hierarchy), where the projections of the minima onto the  $\sin^2 2\theta_{13} - \delta_l$ -plane are shown as diamonds (normal hierarchy) and dots (inverted hierarchy). For the latter, the  $\Delta\chi^2$ -value with respect to the best-fit point is also given. Adopted from [19].

KASKA near detectors will collect 600,000 reactor  $\bar{\nu}_e$  events in three years operation. This will become the highest statistics so far obtained and the observed reactor neutrino spectrum will become the world standard. The measured spectrum can be used to study fission product. Especially there is no calculation of reactor neutrino spectrum at energy  $>8$  MeV which are produced generally by short lifetime  $\beta$ -decay isotopes.

In the future, the reactors  $\bar{\nu}_e$ 's may be used to precisely measure  $\theta_{12}$  by observing the deficit at baseline 50 km, and  $\Delta m_{13}^2$  by observing spectral shape distortion at baseline  $\sim 5$  km. Once such parameters are measured precisely, the electron type neutrinos can be used as a useful tool to probe internal structure of the sun, supernova explosion mechanisms and radiogenic structure of the earth. Because Kashiwazaki-Kariwa nuclear power station is the most intense neutrino source in the world, it is appropriate to use it to measure such parameters. In such an occasion, the KASKA- $\theta_{13}$  detectors can be used as precise near detectors as described in the next section.

## 2 General Description of the Experiment

### 2.1 Kashiwazaki-Kariwa Nuclear Power Station

KASKA is an abbreviation of *Kashiwazaki-Kariwa Nuclear Power Station*, following the tradition to name the experiment after the power station to use. The Kashiwazaki-Kariwa nuclear power station [20], owned and operated by Tokyo Electric Power Company (TEPCO), is located 220 km northwest of Tokyo and 60 km south-west of Niigata-city (Fig. 12).

The name of the plant comes from the names of the local area on which the plant site is locate, Kashiwazaki-city and Kariwa-village. Fig. 13 shows a picture of the power station. The plant site has an area of 4.2 square kilometers, approximately 1.5 km wide and 3 km long. The Kashiwazaki-Kariwa power station has 7 reactors which have a total capacity of world's largest thermal energy of 24.3GW. The reactors are numbered, from south-west to north-east, as #1,#2, #3, #4 and #7, #6, #5. These reactors are arranged approximately in a line forming two clusters, each consisting of 4 and 3 reactors. The distance between the two clusters is  $\sim 1.5$  km. Fig. 14 compares the thermal powers of the proposed reactor  $\theta_{13}$  projects in the world. Kashiwazaki-Kariwa nuclear power station is the most powerful neutrino sources, producing an Avogadro number of  $\bar{\nu}_e$ 's in every 2 minutes when all the reactors are operating. The reactor #1 through #5 is the conventional boiling light water reactors (BWR) and #6, #7 are advanced BWRs (ABWR). Table 1 and 2 summarize the reactor parameters.

The newest reactor will be more than 10 years old when KASKA is expected to start data taking. Therefore all the reactor fuel is well in equilibrium state and average neutrino flux per unit power and energy spectrum are stable.

The reactor operator TEPCO is very much supportive for basic research. KASKA group performed a boring study in the site of Kashiwazaki-Kariwa nuclear power station at the site of near detector in the fall of 2004. TEPCO





Figure 12: Location of the Kashiwazaki Kariwa nuclear power station. [20]



Figure 13: Aerial view of the Kashiwazaki Kariwa Nuclear Power Station. [21]

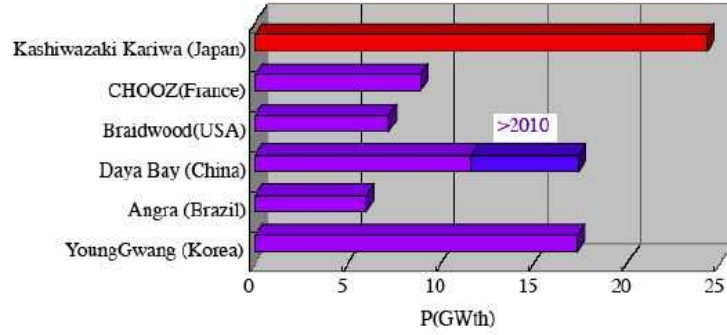


Figure 14: Site powers for reactor  $\theta_{13}$  experiments.

Table 1: Kashiwazaki-Kariwa Reactor Parameters[22]

#	Type	Thermal Power (GWth)	Start Operation
1	BWR5	3.293	1985.09.18
2	BWR5	3.293	1990.09.28
3	BWR5	3.293	1993.08.11
4	BWR5	3.293	1994.08.11
5	BWR5	3.293	1990.04.10
6	ABWR	3.926	1996.11.07
7	ABWR	3.926	1997.07.02

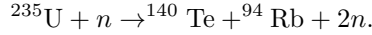
Table 2: BWR, ABWR parameters[22]

#	BWR5	ABWR
Thermal Power	3.293(GWth)	3.926(GWth)
Electric Power	1.067(GWe)	1.315(GWe)
Fuel Inventory	132tHM	150tHM
Active Core Height	3.71m	3.71m
Active Core Diameter	4.75m	5.16m
Fuel	UO <sub>2</sub> pellet	UO <sub>2</sub> pellet
Cycle length	13months	13months
Fraction of Core Reloaded Each Cycle	25%	25%
Enrichment	3.4%	3.5%

and the power station helped much of our activities in the site.

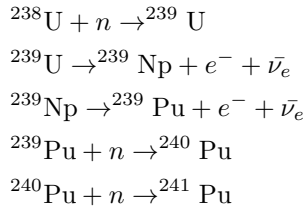
## 2.2 Reactor Neutrinos

In reactors, the power is generated in fission reactions of fissile elements such as uranium and plutonium. An example of fission reaction is shown below.



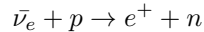
The fission products are generally neutron rich nuclei and perform several  $\beta$  decays before they become stable nuclei. 6  $\beta$ -decays take place in average per fission, which means 6  $\bar{\nu}_e$ 's are produced per fission along with 200 MeV of energy release, resulting in production of  $5 \times 10^{21} \bar{\nu}_e$  per second for Kashiwazaki-Kariwa nuclear power station.

The component of reactor fuel changes along with 'burn-up' through neutron absorption and beta decay processes as well as the fission reactions. Below shows an example of plutonium production scheme.



$^{239}\text{Pu}$  and  $^{241}\text{Pu}$  produced are also fissile elements and contribute to the power and neutrino generation.  $^{238}\text{U}$  performs fission reaction after absorbing energetic neutrons. Fig. 15 shows an example of change of the fuel components caused by the burn-up effect for the case of constant neutron flux.  $^{235}\text{U}$ ,  $^{238}\text{U}$ ,  $^{239}\text{Pu}$  and  $^{241}\text{Pu}$  contribute more than 99.9% of the fission reactions. Fig. 16 shows the neutrino spectrum for the four main components[23]. Because the neutrino spectra depends on fission element, the energy spectrum of the neutrinos from reactor changes along with the burn-up. The fuel exchange takes place approximately once per year, in which 1/4 of old fuel rods are replaced to new ones. The fuels of all the Kashiwazaki-Kariwa reactors are in equilibrium stage, that is 1/4 of the fuel is new and 1/4 of the fuel is 1 year old, 1/4 of the fuel is 2 years old and the rest is 3 years old. Thus the component ratio of the fuel and neutrino spectrum is stabilized in time.

In liquid scintillator,  $\bar{\nu}_e$ 's are detected through inverse  $\beta$  decay reaction with protons,



The energy threshold of this reaction is 1.8 MeV and the energies of the  $\bar{\nu}_e$ 's produced in the  $\beta$ -decay of U, Pu, Np and neutron produced in the core are too low to perform the reaction. Because a typical kinetic energy of recoiled

### Time evolution of Fissile Elements

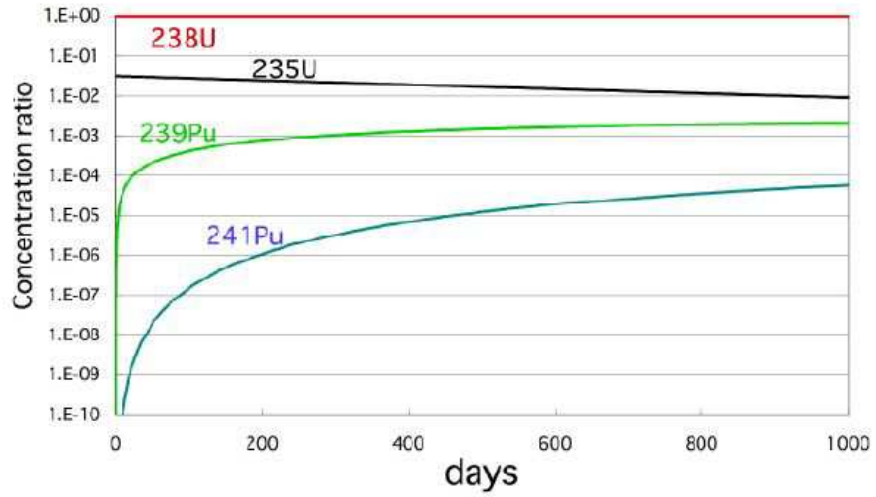


Figure 15: Reactor fuel burn up.

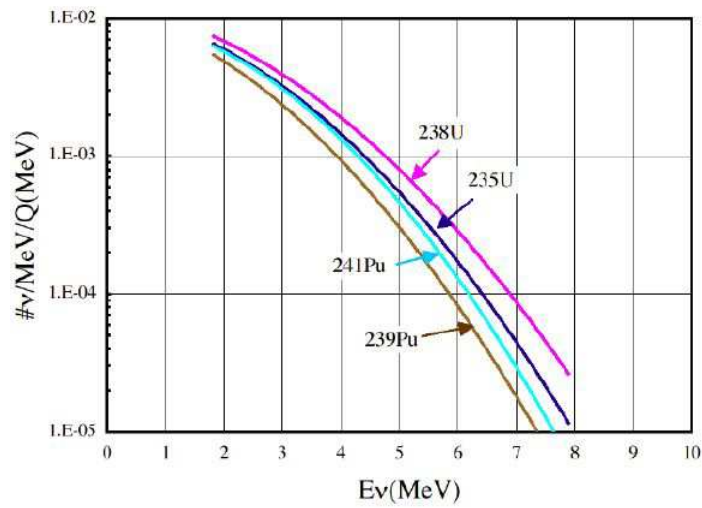


Figure 16: Neutrino spectra for main fission elements

neutron is only a few tens of KeV, the kinetic energy of the positron is  $\bar{\nu}_e$  energy minus 1.8 MeV. The positron annihilates with electron and produces two 0.511 MeV  $\gamma$ 's. Although the lifetime of ortho positronium is 140 ns, the pick-off annihilation takes place within a few nano second [24]. Finally, the visible energy of the event becomes,

$$E_{vis}^{e^+} = E_\nu - 0.78\text{MeV} \quad (11)$$

with a good accuracy. Therefore the neutrino energy and visible energy can be directly connected and the modulation of neutrino energy spectrum due to neutrino oscillation can directly be measured, unlike  $\nu e$  elastic scattering case. Because the reaction is the inverse process of the neutron beta decay, the cross section is closely related to the neutron lifetime  $\tau_n$ ,

$$\sigma_{\nu p} = \frac{2\pi^2 E_e p_e}{1.7152 m_e^5 \tau_n} \approx 9.6 \times 10^{-44} E_e(\text{MeV}) p_e(\text{MeV}/c) [\text{cm}^2] \quad (12)$$

where 1.7152 comes from the phase space factor, including Coulomb, weak magnetism, recoil and outer radiative corrections. Since the  $q^2$  of the reaction is very small compared with nucleon mass scale, the correction is also small and it is known to the precision of 0.2% [25].

The visible energy spectrum in case no neutrino oscillation is calculated as,

$$\mu(E, t) = N_p \frac{P(t)}{4\pi L^2} \sigma_{\nu p}(E) \sum_i f_i(E) n^i(t) \quad (13)$$

where  $P(t)$  is the power generation of the reactor at time  $t$ ,  $L$  is the distance between the detector and the reactor,  $\sigma_{\nu p}(E)$  is the inverse beta decay cross section,  $f_i(E)$  is the neutrino spectrum per fission of element  $i$ ,  $n^i$  is the fission rate per unit power generation, and  $N_p$  is the number of target protons. Due to the burn-up effect  $n^i$  is a function of time. Fig. 17 shows the  $\bar{\nu}_e$  energy spectrum of the  $\bar{\nu}_e p$  signals from the four main elements calculated using data from ref [26]. A typical energy of the detected reactor neutrino is around 4 MeV and typical visible energy is 3 MeV. The ratio of event rate is  $^{235}\text{U}: ^{238}\text{U}: ^{239}\text{Pu}: ^{241}\text{Pu} \sim 1:1.39:0.62:0.88$ . Therefore, when calculating expected number of events, it is necessary to know the fission rate of each fissile element in the reactor cores. Typically the uncertainty of the expected neutrino event rate due to the uncertainty of the fuel components is less than 1%. The neutrino spectrum from each fissile elements are known in such a way that the neutrino detection rate agrees with data at 2.5% of accuracy [23]. The thermal power generation will be provided from the reactor operating company. The error of the thermal power measurement is mainly caused by the flow meter of the cooling water, which is 2% or less. In total, the absolute error of the expected neutrino event is less than 3.4%. However, most of the errors are common for near and far detectors and will cancel out when both data are compared and relative error on oscillation measurement caused from reactor neutrino flux uncertainty is expected to be 0.2% as described in Section 8.

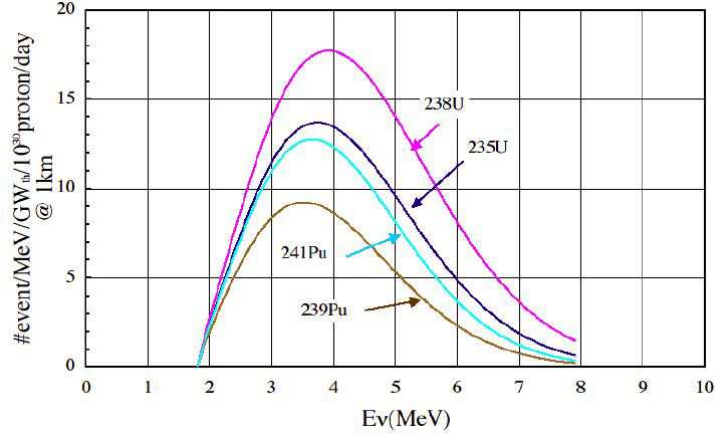


Figure 17: Energy spectrum for detected neutrino ( $f_{\nu}\sigma_{\nu p}$ ). A simple parametrization of reactor neutrinos is used [26].

### 2.3 General Description of Neutrino Detector

In KASKA experiment, four neutrino detectors with an identical structure will be used. Two near detectors are placed in shaft halls at approximate distances of 350~400 m from respective reactor cluster and two far detectors are placed in a shaft hole at a distance of  $\sim 1.6$  km from all the reactors. Fig. 18 shows relative reactor and detector positions. By comparing the data of near and far detectors, most of the systematic errors such as detection efficiency and neutrino flux will cancel out as will be described in Section 8. Table 3 shows event and cosmic-ray rate parameters for KASKA and CHOOZ detectors. Although the KASKA-far

Table 3: Baseline, event rate and cosmic-ray background ratio. The reactor operation, event selection and live-time efficiencies reduce neutrino signal rate roughly half.

Detector	target mass (ton)	Average Baseline (km)	Thermal Power ( $\text{GW}_{th}$ )	Event rate (/day)	Depth (mwe)	$\nu/\mu$ ratio
KASKA-A	6	0.4	13.2	520	90	1.4
-B	6	0.35	11.1	570	90	1.6
-C	$6 \times 2$	1.6	24.3	$60 \times 2$	260	1
CHOOZ	5	1.07	8.5	40	300	0.9

baseline is significantly longer than CHOOZ one and the depth is shallower, the ratio of neutrino flux and cosmic-ray rate becomes better thanks to the

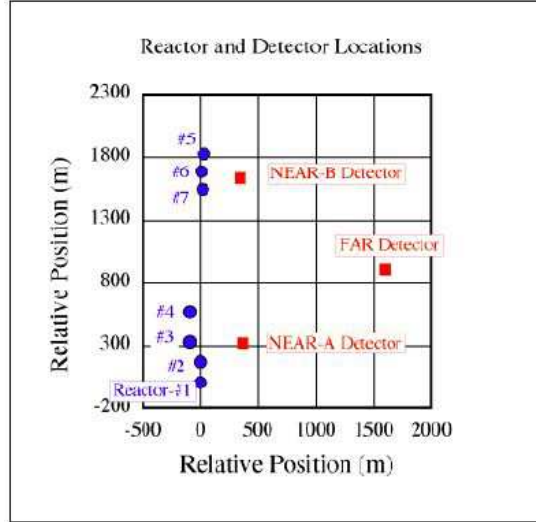


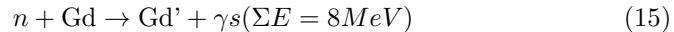
Figure 18: Reactor and detector relative positions.

high power of the power station. Moreover, KASKA detectors have thicker buffer layers and the background is expected to be significantly improves from CHOOZ.

Fig. 19 shows a schematic view of the detector. The central part (Region-I) is 6 tons of Gadolinium loaded liquid scintillator (Gd-LS). A candidate LS is a PaloVerde type [27], which was successfully used in acrylic containers. The liquid scintillator is pseudocumene and mineral oil base with 0.1 % Gd concentration, with specific gravity of  $0.8 \text{ g/cm}^2$  and H/C ratio of 1.8. Fig. 20 shows a schematic diagram of the neutrino reaction. The reactor  $\bar{\nu}_e$  is detected in the Gd-LS with the inverse  $\beta$ -decay process.



The positron has kinetic energy of  $E_\nu - 1.8 \text{ MeV}$  and eventually annihilates with an electron, producing two  $0.5 \text{ MeV}$   $\gamma$ 's as described in the previous subsection. The neutron produced has energies of  $O(10 \text{ KeV})$  and is thermalized quickly by colliding with protons and absorbed by Gd. The Gd produces  $8 \text{ MeV}$  cascade  $\gamma$ -rays after the neutron absorption.



Because energies of  $\beta$  and  $\gamma$  rays of natural radio isotopes are lower than  $5 \text{ MeV}$ , the neutron signal is free from such backgrounds. The neutron absorption signal occurs typically  $30 \mu\text{s}$  after the positron signal. The  $\bar{\nu}_e$  event is identified by requiring that both signals occur within  $200 \mu\text{s}$ . With this delayed coincidence technique, the backgrounds are severely suppressed.

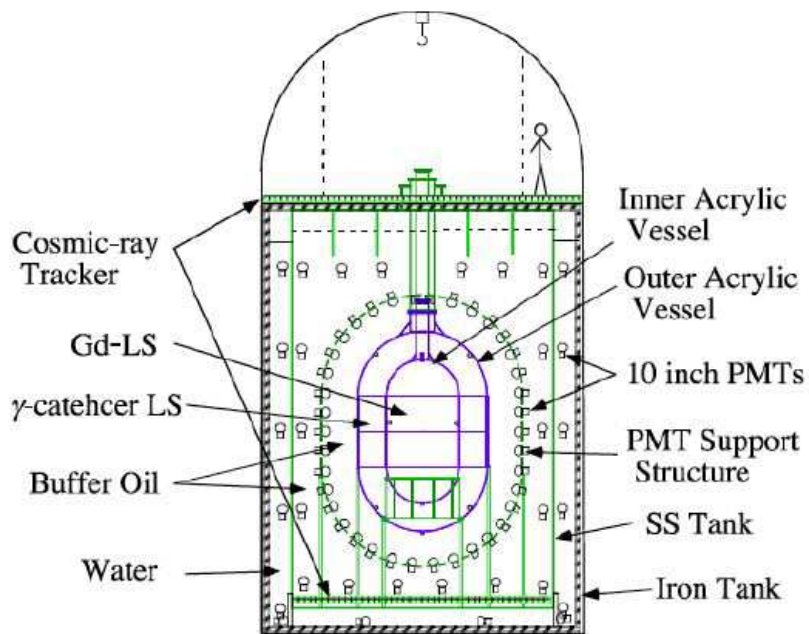


Figure 19: Schematic of the KASKA detector.

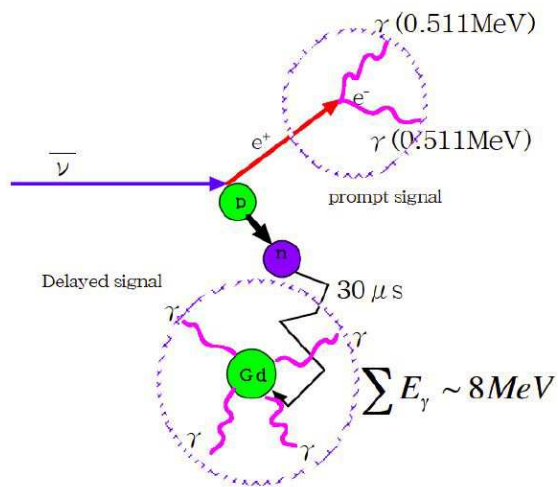


Figure 20: Schematic of neutrino signal



The Gd-LS is contained in an UV-transparent acrylic vessel with a shape of two hemispheres sandwiching a cylinder. The radius of the hemisphere and cylinder is 0.9 m and the height of the cylinder is 1.8 m. There is a 70 cm thick unloaded liquid scintillator layer (Region-II) outside of the Region-I. This region is used to catch the  $\gamma$ -rays which escape from Region-I, and to reconstruct the original energies of Gd and positron signals. Fig. 21 shows the energy spectra of the Gd and positron signals measured by CHOOZ experiment which also has 70 cm  $\gamma$ -catcher region. A clear peak is observed

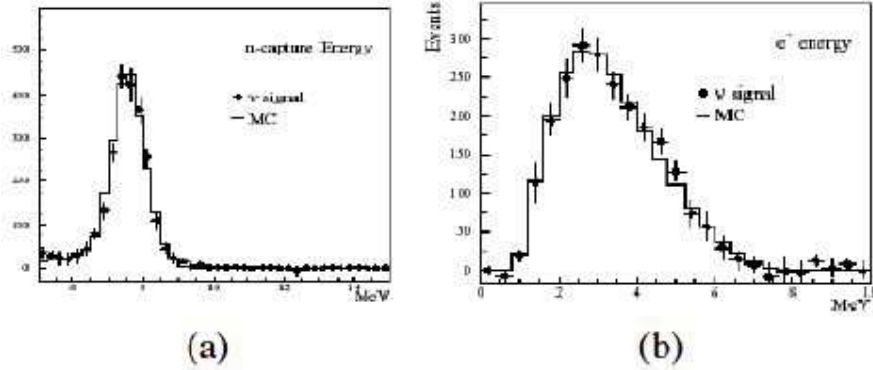


Figure 21: Energy Spectrum of (a) Gd signal and (b) positron signal [10].

in the Gd signal. Because the event rate at the energy threshold ( $=5$  MeV) is small the dependence of the efficiencies on the cut parameter is small. This LS will be formulated by mixing PC, paraffin oils and flours, and light output and specific gravity are adjusted to same as those of Gd-LS. The region-II scintillator is contained in a UV transparent acrylic vessel with the hemisphere-cylinder structure whose radius and cylinder height are 1.6 m and 1.8 m, respectively. There is a buffer oil layer outside region-II which shields liquid scintillators from  $\gamma$ -rays and neutrons coming from outside. A PMT support structure divides the buffer oil at 90 cm distance from the region-II acrylic vessel. The inner part (Region-III) mainly works as  $\gamma$ -ray shield coming from the PMT. The outer buffer part (Region-IV) is used as a  $\gamma$ -ray and neutron shield from detector walls and outer soils, and works as a cosmic-ray veto. In order to improve the cosmic-ray veto efficiency, the buffer oil may be made of a weak scintillator having 10% of light output of Gd-LS. The base oil will be a paraffin oil having a similar specific gravity as region-II scintillator. These oils are contained in a stainless steel tank with a diameter 6.5m and shell thickness 15 mm. There are 300 10-inch low background PMTs looking at the scintillator region, whose photo cathode covers 10% of the surface area. Some LEDs and CCD cameras are also arranged in the tank which are used to monitor the position of calibration devices. Outside of the stainless steel tank is pure water. Water proof PMTs are sub-

merged in the water and work as Cherenkov cosmic-ray veto counter. The water is contained in a hermetic cylindrical iron tank. This tank also works as shield for geo-magnetic field. Outside of these tanks, there are thick iron layers to shield gamma rays from the soils outside. This structure has a leak-safe effect. That is, if a crack should develop in the stainless steel tank, the water outside would come in the oil region and the oil would not come out.

There are cosmic-ray tracking devices at the top and bottom of the detector. The measured cosmic-ray track is used to estimate spallation background such as  $^9\text{Li}$  and  $^8\text{He}$  based on the relation of the position of the events and the track.

In order to reduce the cosmic-ray background, the detectors are placed in deep shaft holes with a diameter of 5 m. The depths are at least 150 m for far detector 50 m for two near detectors.

## 2.4 Sensitivities of KASKA

### 2.4.1 $\sin^2 2\theta_{13}$ measurement

The expected size of the relative systematic error  $\sigma_{\text{rel}}$  on the near-far comparison of KASKA experiment is better than 1%, possibly be 0.5% level. Since the far detectors will collect 70K reactor  $\bar{\nu}_e$  with 3 years of data taking and near detectors will collect 10 times more data, the statistic error becomes 0.4%.

The expected sensitivities for rate only and rate + shape analysis are shown in the Fig. 22. If no deficit is observed, it is possible to set upper limit on  $\sin^2 2\theta_{13}$  at 0.015 to 0.020. This sensitivity is 10 times better than the CHOOZ limit. The sensitivity at  $\Delta m^2 > 0.01\text{eV}^2$  comes from test of the deficit of  $\bar{\nu}_e$  flux measured by the near detectors. Because the absolute systematic error and statistics error are smaller than previous experiments a sterile neutrino search can be performed in this region.

If the true value of  $\sin^2 2\theta_{13}$  is 0.04 or 0.1, for example, and future long baseline experiments show  $\Delta m_{31}^2 = 2.5 \times 10^{-3}\text{eV}^2$ , rate-only analysis constrains  $\sin^2 2\theta_{13}$  with 1 degree of freedom (d.o.f.) analysis as shown in Fig. 23. Results with rate+shape analysis are shown in Fig. 2.4.1. Note that the width of the region has the meaning on the line of  $\Delta m_{31}^2 = 2.5 \times 10^{-3}\text{eV}^2$  only because of 1 d.o.f. analysis.

If a finite  $\sin^2 2\theta_{13}$  is observed by KASKA experiment it means that the parameter is reasonably large and there is a good chance to observe leptonic CP violation parameter  $\delta_l$  from asymmetry of the probability of  $\nu_\mu \rightarrow \nu_e$  and  $\bar{\nu}_\mu \rightarrow \bar{\nu}_e$  appearances in future accelerator based long baseline experiment. If  $\sin^2 2\theta_{13}$  is too small to be detected by KASKA, it means it is difficult to observe  $\delta_l$  and more sensitive experiments to pin down  $\sin^2 2\theta_{13}$  will be necessary before proceeding to accelerator based  $\delta_l$  experiments.

### 2.4.2 High statistics reactor $\bar{\nu}_e$ measurement

The KASKA near detectors will collect 600,000 reactor  $\bar{\nu}_e$  events. This will be the highest statistics of reactor  $\bar{\nu}_e$  detection. Table 4 compares the statistics

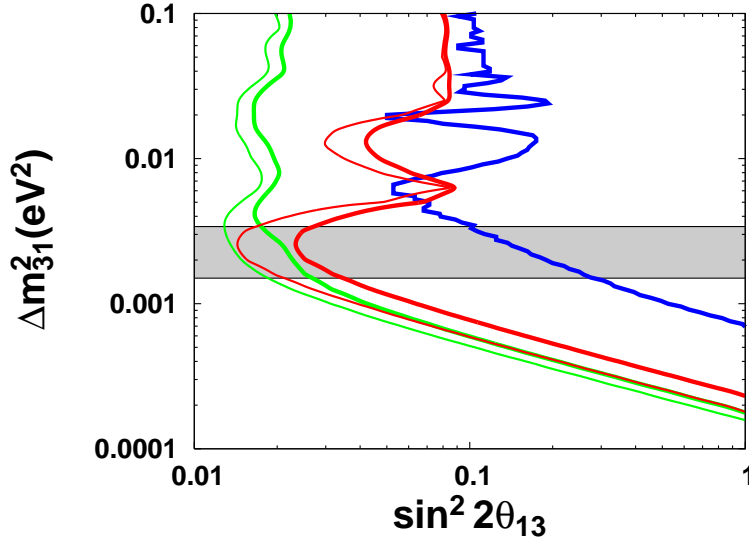


Figure 22: 90% CL sensitivity to  $\sin^2 2\theta_{13}$  in KASKA is shown with the analysis for 1 degree of freedom. Red curves are of the rate analysis, and thin and bold ones are obtained with 0.5% and 1% relative errors in the near-far comparison, respectively. 2.5% error on the flux is included in the analysis also. Green curves are of the rate+shape analysis with 14 bins within  $1.8\text{MeV} \leq E_\nu \leq 8.8\text{MeV}$ . 0.5% (1%) uncorrelated relative error between detectors is assumed to be divided into 0.5% (1%) uncorrelated error between bins and 0.5% (1%) correlated one. The similar assumption is used for 2.5% error on the flux also. The blue curve shows the bound by the CHOOZ experiment with the analysis for 2 degrees of freedom. The shaded region corresponds to 90%CL allowed region by the atmospheric neutrino measurement in SK-I:  $1.5 \times 10^{-3}\text{eV}^2 \leq \Delta m^2 \leq 3.4 \times 10^{-3}\text{eV}^2$

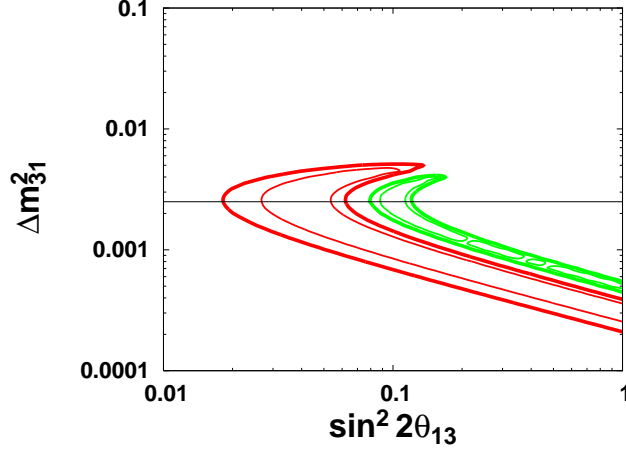


Figure 23: Shown are the constraints on  $\sin^2 2\theta_{13}$  to be obtained by the rate analysis in the KASKA experiment. The true value of  $\sin^2 2\theta_{13}$  is assumed to be 0.04 (red) or 0.1 (green).  $\Delta m_{31}^2$  is assumed to be known precisely by the future long baseline experiments as  $\Delta m_{31}^2 = 2.5 \times 10^{-3} \text{eV}^2$ . The thin and bold curves are obtained by  $\sigma_{\text{rel}} = 0.05\%$  and  $0.1\%$ , respectively.

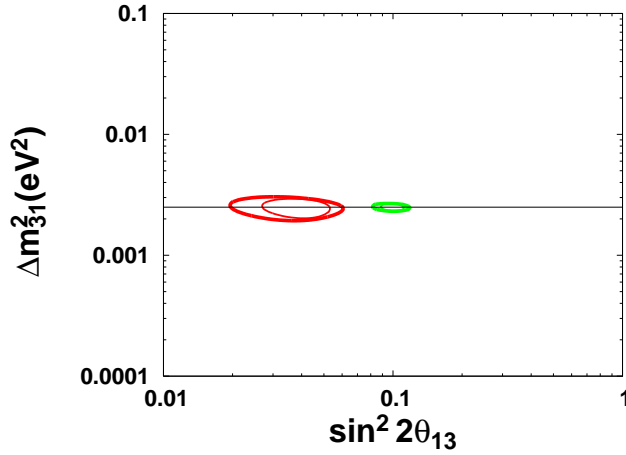


Figure 24: Shown are the constraints on  $\sin^2 2\theta_{13}$  to be obtained by the rate+shape analysis in the KASKA experiment. The true value of  $\sin^2 2\theta_{13}$  is assumed to be 0.04 (red) or 0.1 (blue).  $\Delta m_{31}^2$  is assumed to be known precisely by the future long baseline experiments as  $\Delta m_{31}^2 = 2.5 \times 10^{-3} \text{eV}^2$ . The thin and bold curves are obtained by the different sizes of systematic errors which are the same as the values used in Fig. 23.

and detector related absolute uncertainties of various experiments. The absolute size of the detector related systematic error in KASKA is less than 1.5 % thanks to the no fiducial volume cut and low backgrounds. Therefore the data taken by KASKA will become standard neutrino  $\bar{\nu}_e$  spectrum and contribute to other reactor  $\bar{\nu}_e$  experiments.

Experiments	# events (N)	$1/\sqrt{N}$ (%)	Detector related Syst. error (%)	Distance(m)
KASKA Nears	600,000	0.13	< 1.5	350, 400
CHOOZ [10]	2,700	1.9	1.8	1050
PaloVerde [11]	1,700	2.4	4.9	750, 890
Bugey [28]	150,000	0.26	4.0	15, 40, 95
Goesgen [29]	30,000	0.57	6	37.9, 45.9, 64.7

Table 4: Comparison of high statistics measurements of the reactor  $\bar{\nu}_e$  flux.

A special situation of KASKA is that because 25 % of KamLAND  $\bar{\nu}_e$  come from Kashiwazaki-Kariwa nuclear power station, the KASKA near detectors work as near detectors for KamLAND and neutrino flux related error of KamLAND can partially be cancelled. This effect improves  $\sin^2 2\theta_{12}$  error, together with removal of uncertainty of the  $\cos^4 \theta_{13}$  term by  $\sin^2 2\theta_{13}$  measurement.

## 2.5 Possible Future Extensions of the KASKA project

Because Kashiwazaki-Kariwa nuclear power station generates the highest  $\bar{\nu}_e$  luminosity in the world, there are a number of opportunities to perform neutrino studies with the best precision.

### 2.5.1 KASKA-II: Detecting non-0 $\delta_l$

In order to proceed to an experiment with errors better than 0.5% level, 12 tons of the far detector mass is not enough. A 50 tons of detectors and deeper shaft holes are under consideration for a next generation KASKA experiment (KASKA-II). By combining KASKA-II and data from Super-JHF or Hyper Kamiokande, there is a chance to identify non-0  $\sin \delta_l$  before proceeding to  $\bar{\nu}_\mu$  beam if  $|\sin \delta_l|$  is reasonably large. Fig. 25 shows the regions in which  $\sin \delta_l$  is consistent with 0. Therefore, it is possible to identify non-0  $\sin \delta_l$  if the nature chooses the values outside of these regions such as  $\sin^2 2\theta_{13} > 0.05$  and  $|\delta_l| > 0.3\pi$  [34].

### 2.5.2 KASKA- $\theta_{12}$ : Accurate $\sin^2 2\theta_{12}$ measurement

$\sin^2 2\theta_{12}$  governs oscillation of the electron type neutrinos at large L/E range. Natural neutrino sources, such as the sun, the earth, supernovae, etc. are sources of electron type neutrinos. Although  $\sin^2 2\theta_{12}$  has been measured by KamLAND

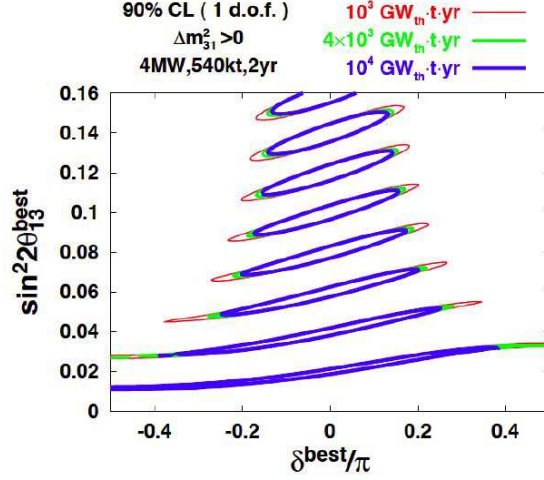


Figure 25:  $\sin \delta_l$  sensitivity by the combination of KASKA-II, Super-JHF (4MW), and Hyper Kamiokande (540kton fiducial mass) [34]. The curves show the regions in which data mimics  $\delta_l = 0$ . If true values of  $\theta_{13}$  and  $\delta_l$  exist outside of all of these regions, we can find that  $\delta_l$  has non-zero value. The sign of  $\Delta m_{31}^2$  is assumed to have been determined by then.

and solar neutrino experiments, further precision measurement is important because it can be used as an inevitable tool to investigate inside of the sun etc.

Another importance of the precise measurement of  $\sin^2 2\theta_{12}$  appears in the relation between the absolute mass of neutrinos and the neutrino-less double beta decay searches; The decay is possible for the Majorana neutrino but impossible for the Dirac neutrino. The absolute mass can not be determined by oscillation experiments because oscillations depend on  $\Delta m_{ij}^2 \equiv m_i^2 - m_j^2$  but are independent of the absolute mass. The information on the absolute mass can be obtained by the Cosmological Microwave Background measurements [30], the tritium beta decay measurements [31], and the neutrino-less double beta decay searches [32]. The upper bound on the effective neutrino mass of the neutrino-less double beta decay can be translated into the upper bound on the absolute mass of Majorana neutrinos. The translation, however, depends on the value of  $\theta_{12}$  very much as we see in Fig. 26. Thus, it is important to know the precise value of  $\sin^2 2\theta_{12}$  in order to extract better information on the absolute mass from the result of experiments of the neutrino-less double beta decay. If we put KamLAND size detector (1 kton) at a distance  $\simeq 50$  km from Kashiwazaki-Kariwa nuclear power station, which corresponds to the oscillation maximum of  $\Delta m_{12}^2$ , it is possible to measure  $\sin^2 2\theta_{12}$  with the highest precision compared with solar-pp neutrino experiments. The KASKA- $\theta_{13}$  detectors can be used as the precise near detectors. Table 5 shows a table taken from the reference [33] in which KASKA- $\theta_{12}$  is referred to as the SADO experiment. It shows that with

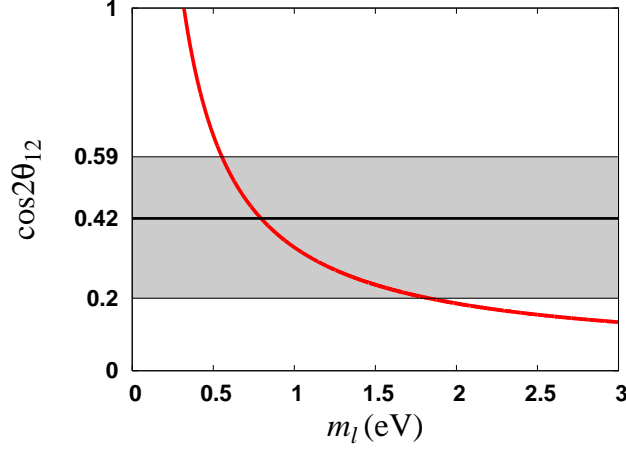


Figure 26: The figure shows the relation between  $\cos 2\theta_{12}$  and the upper bound on the mass of the lightest neutrino for a given upper bound (0.1eV is used as an example) on the effective neutrino mass of the neutrino-less double beta decay. The shaded region corresponds the 99.73%CL allowed region of  $\cos 2\theta_{12}$  obtained by the combined analysis with solar neutrino and KamLAND results under the assumption of CPT invariance.

KASKA- $\theta_{12}$  configuration, it is possible to measure  $\sin^2 \theta_{12}$  with 2.4% precision. In this measurement, background from geo-neutrino is a main issue to obtain the highest sensitivity because energy cut introduces large systematics. Note that large detector size does not help to reduce geo-neutrino background and to obtain a good S/N ratio. One merit of KASKA- $\theta_{12}$  is a good S/N ratio by virtue of the high reactor power. Another merit of KASKA- $\theta_{12}$  is that the error on the estimation of the geo-neutrino background can be reduced by the help of the KamLAND experiment which will have measured the geo-neutrino flux of which large part of the sources is common.

Experiments	$\delta s_{12}^2/s_{12}^2$ at 68.27% CL	$\delta s_{12}^2/s_{12}^2$ at 99.73% CL
Solar+ KL (present)	8 %	26 %
Solar+ KL (3 yr)	7 %	20 %
Solar+ KL (3 yr) + pp (1%)	4 %	11 %
54 km		
SADO for 10 GWth·kt·yr	4.6 % (5.0 %)	12.2 % (12.9 %)
SADO for 20 GWth·kt·yr	3.4 % (3.8 %)	8.8 % (9.5 %)
SADO for 60 GWth·kt·yr	2.1 % (2.4 %)	5.5 % (6.2 %)

Table 5:

### 2.5.3 KASKA- $\Delta m_{13}^2$ : Independent $\Delta m_{13}^2$ measurement

For the case of three generations neutrino, we have  $\Delta m_{13}^2 \approx \Delta m_{23}^2$ . However it is an important item which has to be tested. If a middle size detector is placed at around 5 km from Kashiwazaki-Kariwa nuclear power station, several cycles of oscillation can be observed in its energy spectrum. It is possible to measure

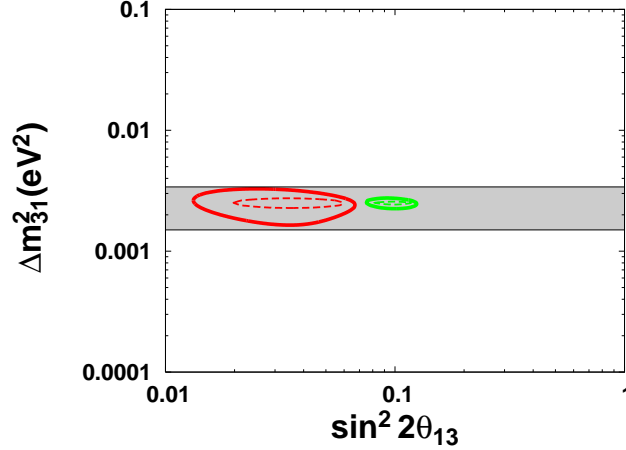


Figure 27: The solid and dashed lines show the 90%CL allowed regions which can be obtained by the KASKA experiment without and with an additional 120 ton detector at 5 km from Kashiwazaki-Kariwa nuclear power station, respectively. The allowed regions are obtained in the analysis for 2 degrees of freedom in order to extract the information on  $\Delta m_{31}^2$ . Red and green curves are for the case that the true value of  $\sin^2 2\theta_{13}$  is 0.04 and 0.1, respectively. The true value of  $\Delta m_{31}^2$  is assumed to be  $2.5 \times 10^{-3} \text{eV}^2$ . The shaded region corresponds to 90%CL allowed region by the atmospheric neutrino measurement in SK-I:  $1.5 \times 10^{-3} \text{eV}^2 \leq \Delta m_{32}^2 \leq 3.4 \times 10^{-3} \text{eV}^2$ .

$\Delta m_{13}^2$  precisely from the spectrum analysis of the modulation. Fig. 27 shows the allowed regions for the positive result in the KASKA experiment with an additional 120 ton detector at 5 km from Kashiwazaki-Kariwa nuclear power station. The precision of  $\Delta m_{13}^2$  is comparable or better than that of the current  $\Delta m_{23}^2$  measurement if  $\sin^2 2\theta_{13}$  is relatively large. Again, the KASKA- $\theta_{13}$  data can be used as precise reference spectrum.

Thus, extensions of KASKA experiment make it possible to measure the oscillation parameters of electron type neutrinos by exploiting the large power of Kashiwazaki-Kariwa nuclear power station as depicted in Fig. 28.



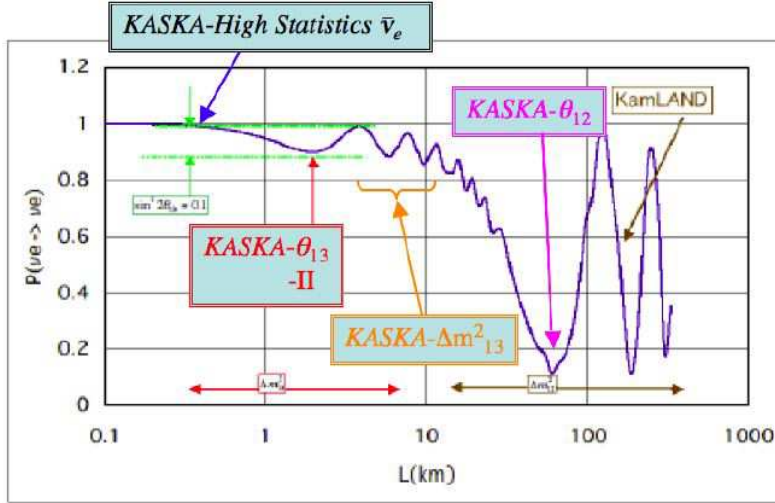


Figure 28: Scope of KASKA experiments. High statistics measurements of reactor  $\bar{\nu}_e$  spectrum with near detectors. High accuracy  $\theta_{13}$  measurements at  $L \sim 1.6$  km. Precise measurement of  $\Delta m_{13}^2$  at  $L \sim 5$  km and precise measurement of  $\theta_{12}$  at  $L \sim 50$  km.

### 3 Detector

#### 3.1 Mechanical Structure

Fig. 19 shows a schematic view of the KASKA detector and Fig. 29 shows mechanical structure and size. The detector consists of inner acrylic vessel to hold the gadolinium loaded liquid scintillator, outer acrylic vessel to hold the  $\gamma$ -catcher scintillator, PMT support frame made of stainless steel, cylindrical stainless steel tank to hold the buffer oil and cylindrical iron tank to hold the water. The shape of acrylic vessels and PMT support frame consists of two hemispheres sandwiching a cylinder part. The radius of the hemisphere is 90 cm, 160 cm and 250 cm for inner acrylic, outer acrylic and PMT support, respectively. The height of the cylinder part is common, 180 cm. Fig. 30 shows the structure of the acrylic vessels. The thickness of the acrylic is 1 cm for inner vessel and 1.5 cm for outer vessel. The acrylic is a UV transparent type. The weight of the acrylic is 0.24 ton for inner and 0.90 ton for outer. The inner volume is 7.6 m<sup>3</sup> for inner vessel and 32 m<sup>3</sup> for outer vessel. Compatibility of acrylic with liquid scintillator is being tested intensively. The inner acrylic vessel is made in a factory and transported to the experimental site and brought down to the detector hall. The outer acrylic vessel is divided into two hemispheres and two 90 cm-high cylinders. Those units are carried to the experimental site by a truck and brought down the shaft hole and assembled in the detector pit.

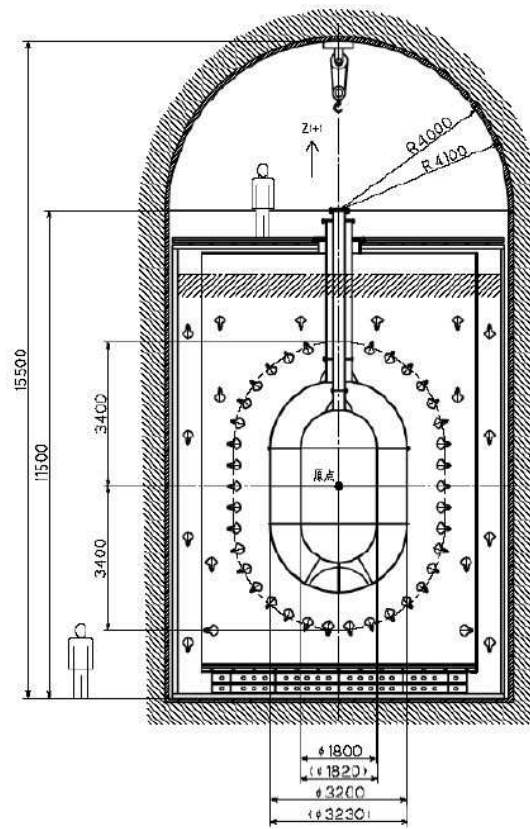


Figure 29: Detector Structure of one unit.

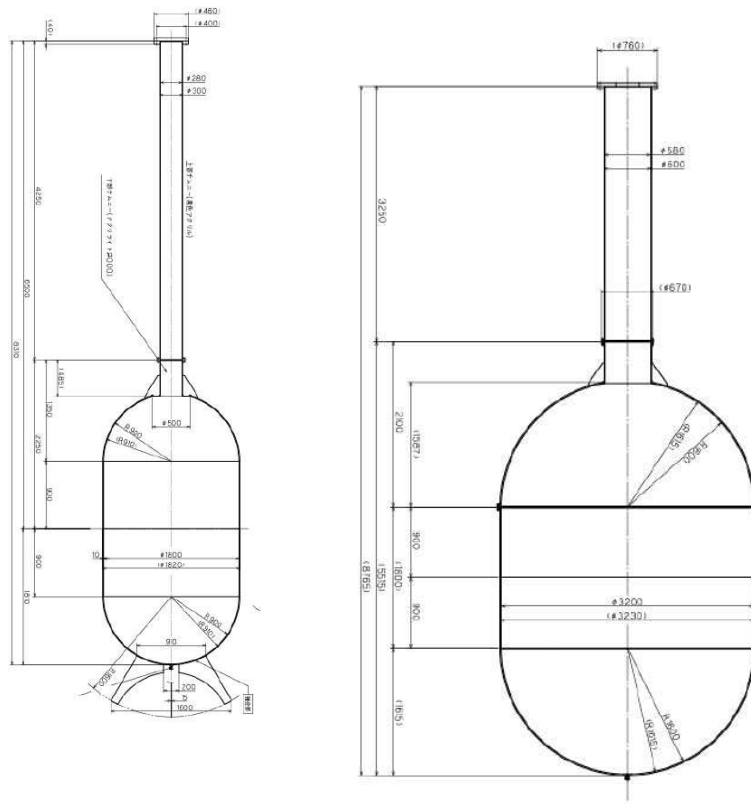


Figure 30: Acrylic Vessels

There are chimneys with 30 cm diameter (inner vessel) and 60 cm (outer vessel), which are to be used to put calibration devices in and to control the liquid level. The chimneys are made of black acrylic.

The PMT support frame has a jungle-gym type structure. The number of PMT is  $\sim 300$  and 1.5 tons of buoyancy force of the PMTs will pull the structure up when the oil is full. The PMT support structure has counter weights to cancel this buoyancy force.

The diameter of the stainless steel cylindrical tank is 6.5 m and the height is 990 cm and the the volume is  $330 \text{ m}^3$ . The thickness of stainless steel cylindrical tank is 15 mm and its total weight is 32 tons. This tank holds 260 tons of oils. The tank has to strong enough to self-stand when the water around is empty while endure the buoyancy force of  $\sim 20$  ton when the water is full.

The diameter of the cylindrical iron tank is 7.5 m and the height is 1,060 cm and the inner volume is  $470 \text{ m}^3$ . The thickness is 11 cm to shield  $\gamma$ -rays coming from outside. It is considered to make this iron tank as geo-magnetic shield by de-magnetizing the iron. Table 6 summarizes detector parameter structures.

Table 6: Detector Structure Parameters.

Item	R (cm)	H (cm)	t (cm)	V ( $\text{m}^3$ )	W (ton)
Inner acrylic	90	180	1.0	0.20	0.24
Outer acrylic	160	180	1.5	0.75	0.90
PMT support	250	180	-	-	2
S.S. tank	325	990	1.5	4.0	32
Iron tank	375	1060	11	37	290

R: Radius of cyliner/hemisphere, H: Height of cylinder/cylinder part, t: Thickness of the vessel, V: Volume of the structure material and W: Weight of the vessel.

### 3.2 Liquid Scintillators

The KASKA detector uses four kinds of liquid. From inner to outer,  $\nu$  target scintillator (Region-I),  $\gamma$  catcher scintillator (Region-II), buffer oil (Region-III, IV) and water for cherenkov cosmic-ray anti-counter (Region-V). Table 7 shows components of each candidate liquid.

In the table, BC521 is a commercial liquid scintillator of a Saint-Gobain product [35] with Gd concentration of 0.5%. PC stands for pseudocumene (1,2,4 tri-methyl-benzene ( $\text{C}_6\text{H}_3(\text{CH}_3)_3$ )), TD stands for Tetradecane ( $\text{C}_{14}\text{H}_{30}$ ). v% means % in volume and w% means % in weight. Table 8 shows properties of these liquids along with the mixed ones.

Table 7: Liquid Scintillator Components

Region	Mixture	Volume (m <sup>3</sup> )	Weight (t)
I	PC(20v%)+TD(60v%)+BC521(20v%)	7.6	6.1
II	PC(15v%)+TD(85v%) +PPO(0.6w%)+bis-MSB(0.01w%)	24	19
III+IV	Paraffin oil (+PPO)	300	240
V	pure water	160	160

Table 8: Liquid Properties

liquid	mass (ton)	specific gravity (g/cm <sup>3</sup> )	flash point (°C)	H/C	light output (% anthracene)
BC521 [36]	-	0.89	44	1.314	68
PC	-	0.880	54	1.33	-
TD	-	0.763	99	2.14	-
I	6.1	0.79	49.5	1.8	53
II	19	0.78	76	2.0	53
III+IV	240	0.76	99	2.14	5
V	160	1.00	-	-	-

### 3.2.1 Neutrino Target (Region-I)

The active neutrino target is Gd Loaded liquid scintillator (Gd-LS) with Gd concentration of 0.1 %. A candidate is a PaloVerde type liquid scintillator [37]. This LS is formulated by mixing 20 % of BC521, 20% of PC and 60% of TD. The molecular formula of the Gd in BC521 is 'gadolinium 2-ethylhexanoate';  $\text{Gd}(\text{CH}_3(\text{CH}_2)_3\text{CH}(\text{C}_2\text{H}_5)\text{CO}_2)_3 \cdot x\text{H}_2\text{O}$ . [27]. The light output is 53 % anthracene. Along with 10 % of PMT cathode coverage with its 20 % quantum efficiency, the light yield will be 150 p.e./MeV, which corresponds to statistical energy resolution of

$$\frac{\delta E}{E} \approx \frac{8.2\%}{\sqrt{E(\text{MeV})}} \quad (16)$$

H/C ratio is 1.8 and proton density is  $7.7 \times 10^{28}/\text{m}^3$ . The PaloVerde experiment used this kind of LS contained in 7.4 m long acrylic cells for a few years without problems. TD is chosen as the base solvent because it is mono-molecular paraffin oil and proton density is exactly known. Paraffin oil does not have double bond in its molecular structure and does not absorb scintillation light, and it is immune to oxidization. Because TD and PC are mono-molecular material, the temperature window of the distillation in refinery process is narrow and contamination is intrinsically small. This strategy was very successful in the KamLAND liquid scintillator. TD has higher flash point and slightly larger H/C ratio and specific gravity than dodecane which is successfully used in KamLAND detector. 30 m<sup>3</sup> of the Gd-LS for four detectors will be formulated at the same time and stored in a storage tank in order to make the components of the four detectors same. When filling in the detector, the LS is carried by 200 liter stainless steel drum cans. The weight of each drum can is measured with relative error of <0.3 % using carefully inter-calibrated scales before and after emptying into the detector and the total amount of Gd-LS introduced is measured precisely. The acrylic vessel containing the Gd-LS has a chimney with 30 cm diameter. 1 cm of head level difference corresponds to 0.01% of LS volume difference. By monitoring the head level, precision monitoring of LS volume in the fiducial region can be performed.

### 3.2.2 $\gamma$ -ray catcher (Region-II)

The purpose of this liquid scintillator is to detect the escape gamma rays from region-I and reconstruct original energies of positron annihilation and neutron capture on Gd signal. The light output is adjusted to be the same as Region-I LS. A candidate of this LS is,

$$\text{PC}(15\%)+\text{TD}(85\%)+\text{PPO}(0.6\text{w}\%)+\text{bis-MSB}(0.01\text{w}\%)$$

The specific gravity is slightly smaller than Region-I LS to keep safety of the acrylic vessel. The concentration of PC is reduced from that of Region-I LS to raise the flash point for safety reason.

### 3.2.3 Buffer oil (Region-III&IV)

The purposes of the buffer oil is to shield the liquid scintillators from  $\gamma$ -rays from the PMT glass and outside soils, and to tag the cosmic-rays. 300 m<sup>3</sup> of paraffin oil will be used as the buffer oil. In order to detect stopping muons whose energy is less than the Cherenkov threshold and to improve cosmic-ray veto efficiency a slight light output ( $\sim 10\%$  of Gd-LS light output) may be given to the oil by adding PPO. The specific gravity is slightly smaller than Region-II scintillator.

### 3.2.4 Cosmic-ray veto (Region-V)

Outside of the stainless steel spherical tank is filled with 160 m<sup>3</sup> of pure water. The purpose of this region is to tag the cosmic-rays to veto the cosmic-ray related background and is to shield the  $\gamma$ -rays and neutrons from the soil outside of the cave and concrete to form the cave. The water is kept purified by circulating.

## 3.3 Photosensor

In order to detect the scintillation photons from liquid scintillators, large aperture photomultiplier tubes (PMT's) are used. One of the candidates is Hamamatsu Photonics K.K. (HPK) 10 inches PMT (R7081). In order to obtain necessary photoelectron yield, more than 10% of the photo cathode coverage is necessary and >300 10 inch PMT's are necessary. Fig.-31 shows the shape of the PMT and table 9 shows its specifications. Fig.-31 also shows the quantum

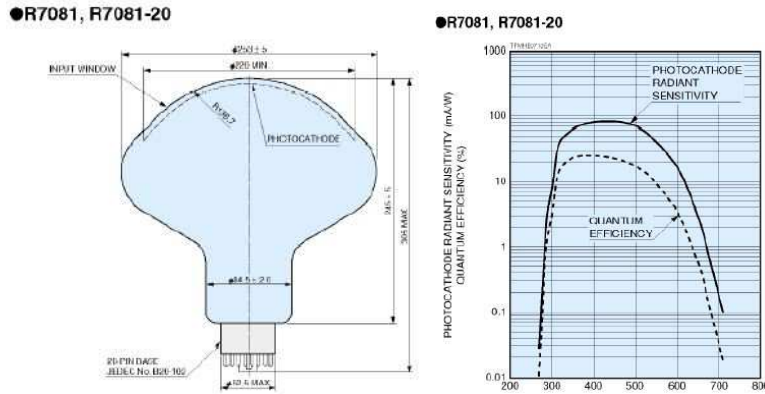


Figure 31: Shape of the PMT envelop and quantum efficiency. [39]

efficiency for the PMT. The photo cathode is bi-Alkali type with 25% quantum efficiency around 400 nm wavelength.

Single photoelectrons response for the PMT was measured as follows. As a light source for this measurement, we used a PiLas picosecond laser light system (=

Table 9: PMT specifications [39]

Type No.	minimum effective area (mm)	Approx. Weight (g)	Q.E. at 390nm (%)	Rise Time (ns)	TTS (ns)
R7081	220	1150	25	4.3	2.9

438.7 nm) having a high precision pulse timing ( $<30$  ps). In order to obtain a single photoelectron response we used neutral density filters to reduce the laser light. For the digitalization of the pulse amplitude we used a LeCroy 2249A ADC. Fig. 32 a) shows the single photoelectron spectrum for R7081. A clean single photoelectron peak can be seen at around 70 ADC channels. Fig. 32 b) shows the leading edge timing for the single photoelectron signals. We used a TDC (Houshin Co. Ltd) for the timing measurement. After a time walk correction using the pulse height information (assuming a square root dependence on the pulse height), a transit-time -spread (TTS) has been obtained to be around 2.5 ns, which is better than the catalogue value of 3.7 ns in which the time walk correction may not be applied. Fig. 32 c) shows the timing distribution after the time walk correction.

One of our worry for the large size PMT's is response uniformity over the large surface area. By changing the laser light incident position, we have measured the pulse height spectra for three different positions. Fig. 33 a) shows the peak ADC channels for single photoelectron spectra measured at three incident positions: 0 (center), 5 cm and 10 cm from the PMT surface center. Data for R5912 are also shown for comparison. Both R5912 and R7081 have a good uniformity within 10 % variance. Fig. 33 b) shows the uniformity of the resolutions (standard deviations). They are also very uniform over the measured surface area. We can conclude from the above measurements that both R5912 and R7081 have enough performance for the detection of the scintillation light.

Generally PMT glass contains significant amounts of radioactive elements and causes single background hits. In order to reduce this background, a low background glass is developed. Table 10 compares the U/Th/K contents of the PMT glass used in various experiments. With this glass and 90 cm of buffer thickness between glass and region-II scintillator, the single rate of the detector will be a few Hz at above 0.7 MeV threshold, which is satisfactory value.

There is an optional idea to install some 2" PMTs besides the 10" PMTs to measure the total energy of cosmic ray signals without saturation problem.

Fig. 34 shows the PMT positions. 300 PMTs are uniformly distributed.

### 3.4 Cosmic-ray Tracking Device

A cosmic-ray tracker system will be installed in the detector. The role of the cosmic-ray tracker is to track the cosmic muon passage which goes through the detector. Spallation background events are estimated by its association to



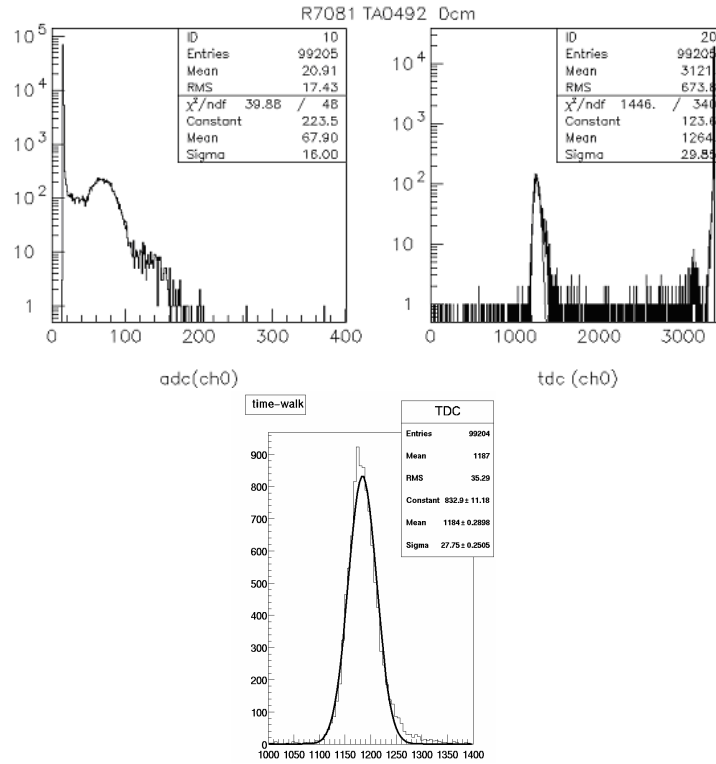


Figure 32: a). Pulse height spectrum and b) leading edge timing distribution for the single photoelectron signals obtained with R7081. c) Timing distribution for R7081 after the time walk correction. The TTS of 2.5 ns is obtained from this figure.

Table 10: radio purity of PMT glasses

Type	$^{238}\text{U}$ (ppm)	$^{232}\text{Th}$ (ppm)	$^{40}\text{K}$ (ppm)	Reference
KASKA candidate	0.046	0.12	0.01	[40]
CHOOZ	0.07	0.1	0.018	[10]
SuperK/KamLAND	0.48	0.47	0.08	[41]
Kamiokande	0.25	0.32	0.016	[41]

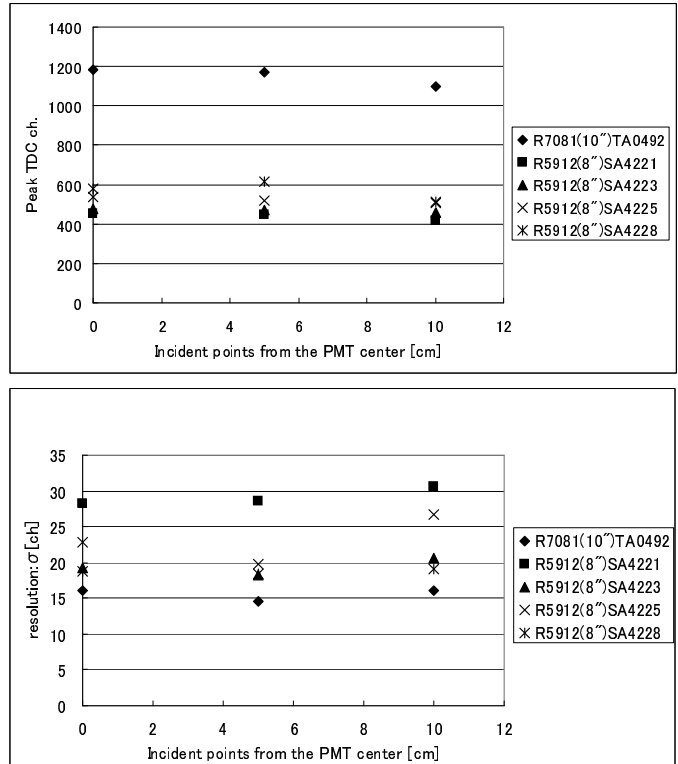


Figure 33: a) Uniformity of the response for three R5912 and one R7081. The incident positions of the laser light were at 0 (center), 5 cm and 10 cm from the PMT surface center. Peak values were stable within 10%. b) Uniformity of the resolution for three R5912 and one R7081.

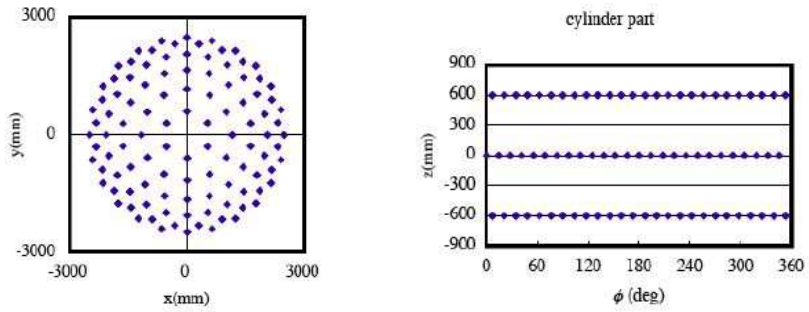


Figure 34: PMT positions. Left: top/bottom view of the hemisphere part. Right: unfolding view of cylinder part.

the cosmic-ray track. The position resolution required is a few centimeters, comparable to or better than the resolution of the vertex reconstruction for the neutrino events in the target region.

To achieve these purposes, several options can be considered for the hardware implementation: use of liquid-scintillator(LS)-based, plastic-scintillator(PS)-based or gaseous detectors such as RPC. In the case of a gaseous detector, building a gas-supplying system down in the shaft hole would be complicated, and some safety issues might arise, too. Not much attention has been paid on this option at this moment.

In cases of LS-based or PS-based detectors, the detector will consist of scintillator strips with a segmentation to match the position resolution. In a design investigated, the scintillator is a rectangular with 10 cm in width, 3 cm in height, and about 5 m in length. In order to cover the whole area of the main detector, about 50 scintillator strips are arranged. A layer consists of two planes, X and Y, which give a 2-dimensional position. Fig.-35 shows the scintillator layer. These two layers are set up on the top and bottom of the main detector. In reality, there have to be some dead spaces to accommodate the mechanical support structure.

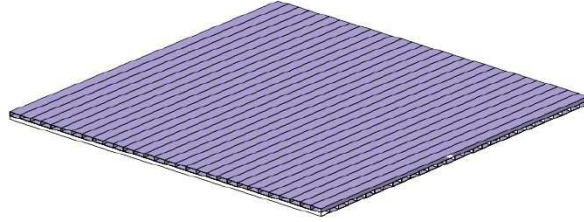


Figure 35: Schematic drawing of a layer of cosmic-ray tracker.

A wavelength-shifting (WLS) fiber is used to transport the scintillation light to the photodetectors such as PMTs. By using the WLS fiber, the photodetector can be set up in a convenient place. The scintillation light is read from both sides. The time difference between both sides will also give a redundant position measurement. The WLS fiber considered is about 1.5 mm in diameter, and a multi-clad type. Because its angle of the total reflection compared with a single-clad type is larger, the light yield is larger as shown in Fig.-36. It is necessary to consider the attenuation length of the WLS fiber. For example, the attenuation length of a multi-clad type fiber, Y11(200)MS made by Kuraray, is about 3.6 meters. The light through the WLS fiber is read by Multi-Anode PMT (MAPMT) such as Hamamatsu H7546 series. The advantage to use MAPMTs is to save the cost, and a smaller occupied space compared with PMTs installed for all cells.

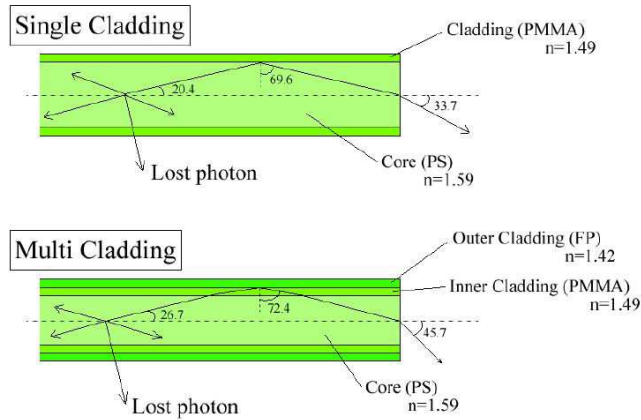


Figure 36: Sketch of Y-11 WLS fiber.

### 3.4.1 A case of LS-based detector

The advantage of this option is low cost scintillator. An aluminum or SUS case and an acrylic cap can be used for the container. UV-transparent acrylic should be used for the cap. There is a ditch on an acrylic cap, and the WLS fiber is inserted as shown in Fig.-37. In this case, it is necessary to consider the attenuation length and light yield because the solid angle of the fiber to absorb the scintillation light is small. Multiple readout fibers may be necessary to collect enough photons.

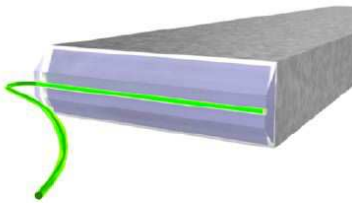


Figure 37: Drawing of an acrylic cap and inserted WLS fiber at the end of a LS-based detector.

### 3.4.2 A case of PS-based detector

In this case, extruded plastic scintillator [38] can be used. This scintillator has inferior optical property, but costs much less than usual PS. The scintillator will be painted on the surface to reflect the light, and a hole will be made to pass the WLS fiber. Extruded PS is used by the SciBar detector at K2K[42]

and by the MINOS experiment [?]. Basic characteristics of this scintillator is shown in table 11. The structure of the plastic scintillator is shown in Fig. 38. WLS fiber is inserted in the center of the scintillator. The advantage is that it is not necessary to consider the attenuation length of scintillator. However, it is necessary to consider the attenuation length of the WLS fiber compared with the case of a LS-based detector.

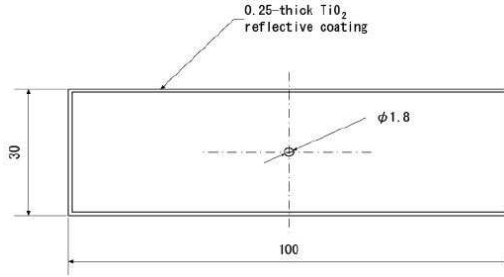


Figure 38: Drawing of an extruded PS strip. The unit is mm.

Table 11: Basic characteristics of the scintillator used in SciBar detector

Scintillator material	polystyrene with PPO (1%) and POPOP (0.03%)
Emission wavelength	420 nm (blue)
Dimensions	$2.5 \times 1.3 \times 300$ cm <sup>3</sup>
Hole diameter	1.8 mm
Reflector material	TiO <sub>2</sub> (15%) infused in polystyrene
Reflector thickness	0.25 mm

## 4 Shaft Hole

The required accuracy on  $\sin^2 2\theta_{13}$  measurement is a fraction of percent. It is necessary to suppress the cosmic-ray related backgrounds significantly to realize such accuracy by placing the detectors deep underground. For KASKA case the far detector should be placed at least 250 meter water equivalent (m.w.e.) deep to sufficiently suppress cosmic ray muons and near detectors should be placed at around 80m.w.e depth. Because there is no mountain around Kashiwazaki-Kariwa nuclear power station for such distances less than 2 km, KASKA uses vertical shaft holes. As the density of the soil in this area is 1.75 g/cm<sup>3</sup>, the physical depth of the shaft holes are 150m for far detector and 50m for near detectors. Fig. 39 shows the schematic of the shaft hole and detector pit under consideration. The diameter of the shaft hole is 5m. A 18m long horizontal

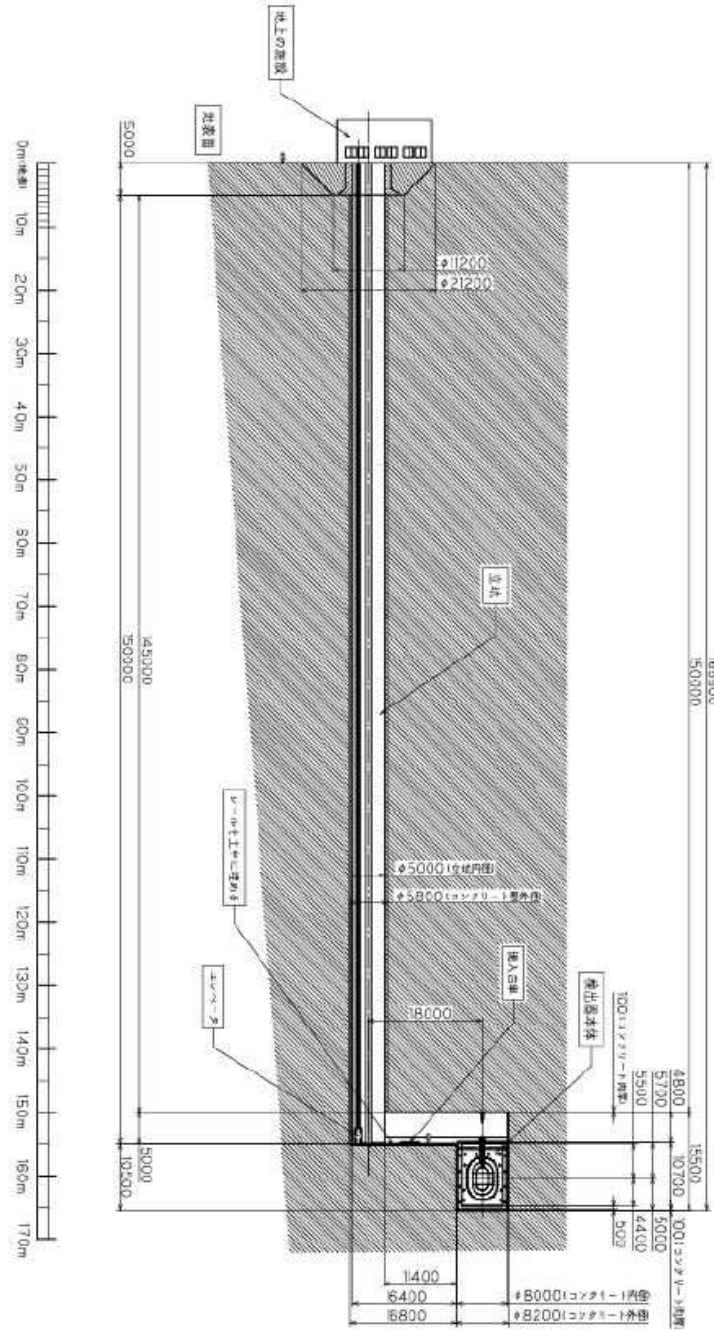


Figure 39: Dimension of a shaft hole for the far detector (one detector case).

corridor connects the shaft hole and the detector pit. The detector pit has a cylindrical hole of 8m diameter and 10m height. The neutrino detector will be placed in the pit. The construction method of the holes will be a short-step method. A few meters are dug down at one time by blasting, then debris are taken out by a crane and then the wall is reinforced by concrete. These procedures are repeated until the hole reaches the target depth. Fig. 4 shows an example of how such construction proceeds. Constructions of such a vertical shaft hole have been performed in several locations. For example, Japan Atomic Energy Association has been digging 1,000m-depth shaft holes with diameter of 4.5m and 6m in parallel for the purpose of studying deep underground storage of nuclear waste. Fig. 4 shows a figure of the twin shaft holes and a picture taken while a shovel car is cleaning the debris. R&D for digging the KASKA holes has been under way. Extensive studies of the geology were performed by the electric power company when the reactors were constructed and overall structure of the geology around this area is well known. Fig. 42 shows stratum at near-B detector position which was measured by our boring study. Table 12 shows the properties of strata.

Table 12: Properties of strata

Name	main constituents	density (g/cm <sup>3</sup> )	water component (%)
Shinki-Saso	fine sand	1.64	5.6
Bansya-Saso	rough sand	1.83	15.1
Yasuda-so	silt, clay	1.76	47.0
Nishiyama-so	silt rock/clay rock	1.74	47.4

The general property of the geology is low density mud with abundant water component. A boring study for the KASKA-B detector was performed in fall 2004. Fig. 4 show a picture taken during the boring study. Sample cores were taken from several depths and properties of the soils, as well as U/Th/K contaminations, have been studied. The cosmic-ray and  $\gamma$ -ray background were also measured at various depths using NaI and plastic scintillators. These information will be used for detailed design of the KASKA neutrino detector.

## 5 Readout Electronics

### 5.1 Property of Signals

The KASKA experiment is composed of four identical detector units each having 300 photomultiplier tubes (PMT), to view the Region-I and II liquid scintillators. Because there are 4 detectors, the total number of PMTs is 1,200. Those signals from the PMTs are read out by flash ADCs (FADC). There also will be hundreds of signals from cosmic-ray anti-counter and cosmic-ray tracking devices. Signals from those devices are readout with conventional ADC/TDC

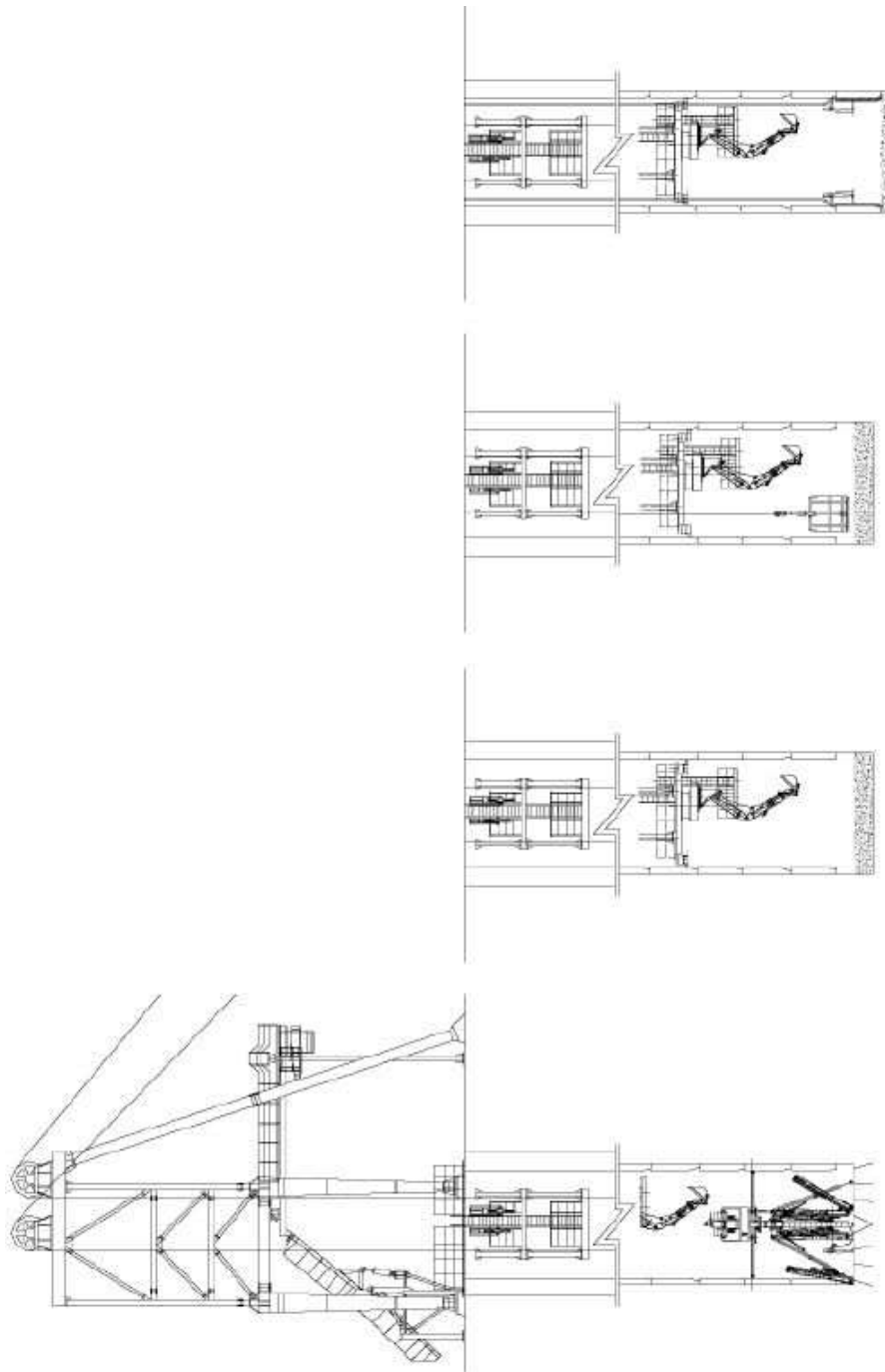


Figure 40: Example of short step excavation procedure. From left to right, drilling/setting an explosive, blasting, taking out debris, moving down/concreting.



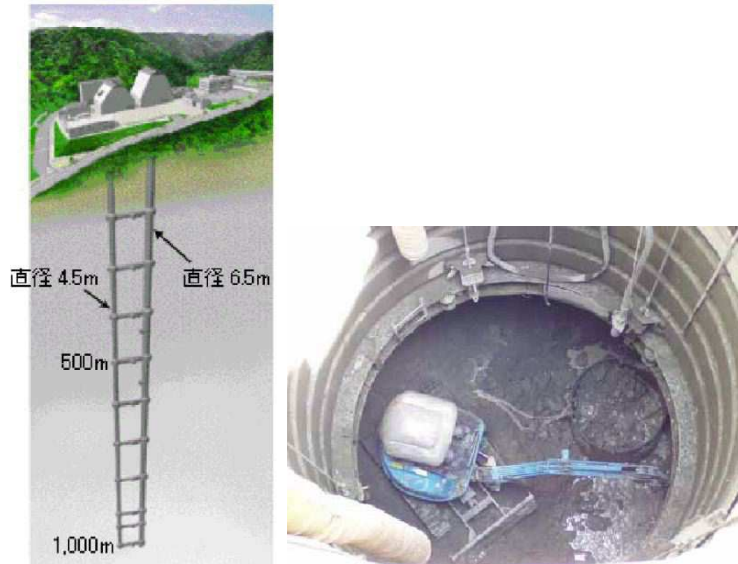


Figure 41: 1000 m depth twin holes and its construction scene [45]

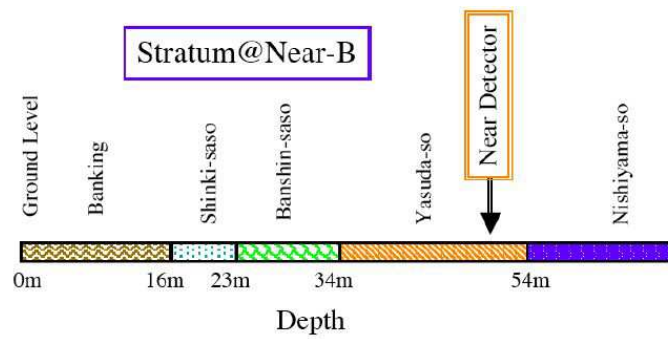


Figure 42: Stratum at near-B detector position, measured by boring study.



Figure 43: Boring study at the near-B site. The towers behind the boring scaffold are ventilation towers of reactor buildings.

systems. The following description concentrates on the readout electronics for the central PMT data, which are being developed for this experiment. Signal sources are anti-neutrino interaction, cosmic rays and other backgrounds and calibration signals. Detection and identification of anti-neutrino is performed by a prompt and a delayed signal generated in an inverse  $\beta$ -decay as described in section (2). The former signal is produced by a positron and the latter is created by  $\gamma$  rays from gadolinium nucleus after absorbing neutron. Fig. 44 shows the conceptual picture of the  $\bar{\nu}_e$  signal.

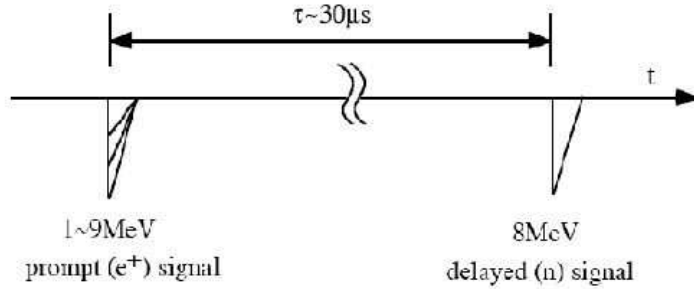


Figure 44: Characteristics of  $\bar{\nu}_e$  signal.

The energy of the prompt signal is 1 to 9 MeV and that of the delayed signal is 8 MeV. The mean interval time of the two signals is about  $30 \mu\text{s}$ . The rates of neutrino signals per detector are  $\sim 1/\text{hour}$  for far detector and  $\sim 10/\text{hour}$  for near detector. The dominant background source is cosmic-ray muons. The maximum energy deposit of the cosmic-ray in the scintillator is 800 MeV for single muon and much more for showering muons. The rate of the cosmic-rays are  $\sim 15 \text{ Hz}$  for far detectors and  $\sim 170 \text{ Hz}$  for near detectors, respectively. The cosmic-ray signal has to be separated from the neutrino signal with very high efficiency for the suppression of backgrounds. An important effect to be considered is production of radioactive elements with spallation reaction. It leaves some radioactivity which remains after the cosmic-ray passing. These activities have to be eliminated from the neutrino signals also. As the energy deposit of the cosmic-ray signals is huge compared with the reactor neutrino signals, the electronics system will be saturated. It is, therefore, necessary to realize fast recovery from cosmic ray signals for the deadtime-less measurement. In addition, there are low energy single background signals which come from radioactive elements in the detector material and soils outside of the tunnel, such U and Th, and their decay chains and also from  $^{40}\text{K}$  and  $^{60}\text{Co}$ , whose visible energy is less than 5 MeV. It is, therefore, expected to be reduced to less than 10 Hz with 0.7 MeV energy threshold by putting a thick absorbing buffer. Finally, the positron produced by stopping muon (Michel positron), whose maximum energy is 53 MeV, will

be used for the calibration in the energy range up to a few 10 MeV.

$$\mu^+ \rightarrow e^+ + \nu_e + \bar{\nu}_\mu$$

As the lifetime of muon is  $2.2\mu s$ , the electronics has to recover quickly from the saturation caused by the initial  $\mu^+$  signal.

Under these circumstances, the requirements for electronics are as follows.

- Measurement of output charge of each PMT hit to reconstruct energies of the signal.
- Measurement of the timing of each PMT hit to reconstruct positions.
- Sufficiently wide dynamic range for neutrino signals and cosmic ray signals.
- Dead-time-less Multi-hit readout capability.
- Measurement of the timing separation between two contiguous events.
- A fast recovery from the saturation of large cosmic-ray signals and monitoring after-muon activities.

In KASKA experiment, most of those information are measured by FADCs, with multi-bank memories for deadtime-less measurement with precise time stamps used to measure the time interval of the prompt and delayed signals.

## 5.2 Electronics Scheme

Fig. 45 shows a schematic diagram of the readout electronics. A signal from the PMT is amplified and put into a 500MHz FADC together with the marker or calibration signals. The output from the FADC is divided into a storage circuit and a trigger circuit. The FADC data going to the storage circuit are recorded in a bank memory of 300 ns equivalent depth, after a digital delay which compensates the latency of the trigger decision. There will be two, or more if necessary, bank memories to eliminate the dead time. When a trigger is issued, the direction of the FADC data flow is switched from a bank to the next one. The newly coming data being digitized are recorded/shifted in the new bank memory, while the stored data in the first bank memory are being readout by a computer. Each bank has a register which holds the data of absolute timing when the trigger is issued. The FADC data for triggering is digitally time-integrated to get the total charge information of the signal. If the total charge exceeds 0.25 p.e. equivalent, the PMT is considered to have a signal and a PMT trigger is issued. This scheme has been proven to work with latency of  $\sim 80$  ns for a prototype. Then a PMT trigger information is sent to a trigger decision module, where the number of hits from all the PMTs is counted up. If the number of hit PMTs exceeds 0.7 MeV threshold, a global trigger is issued, which is sent to a trigger control circuit. The trigger control combines the amplitude and timing information of the data and decides if the currently

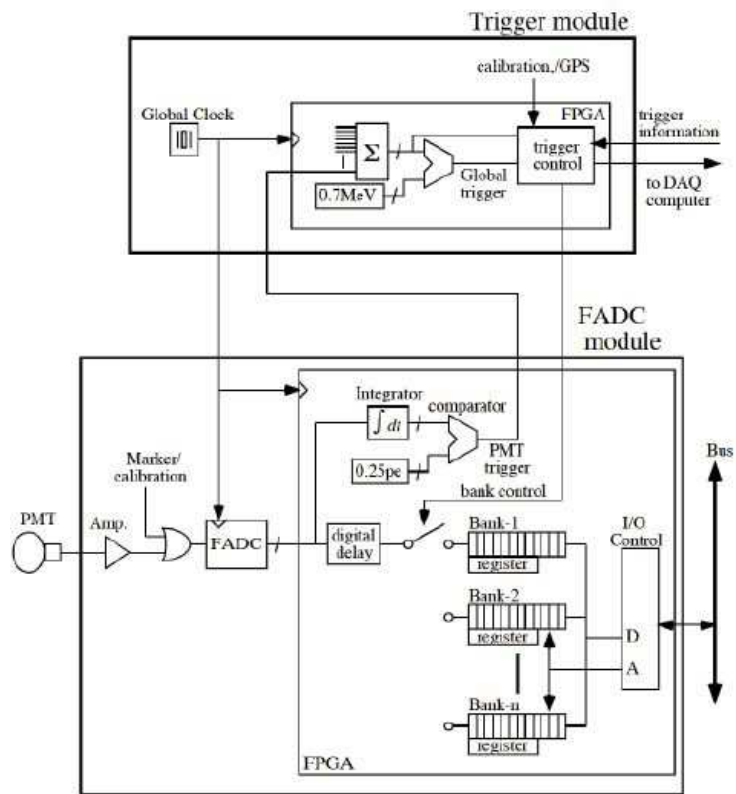


Figure 45: Schematics of KASKA electronics.

active bank is switched and send information about which bank to read out to the data acquisition computer.

Followings are assumed KASKA detector parameters and the properties of signals for the rough estimate of necessary gain and dynamic range which are required for the electronics.

#### 1. KASKA detector parameters

- Required energy loss for one photon in the scintillator: 150 eV  
⇒ 46% Anthracene equivalent.
- PMT photocathode diameter: 22 cm.
- Radius of photocathode position in detector: 3 m  
⇒ photocathode coverage=10 %.
- Radius of the region-I scintillator: 1.4 m.
- Quantum efficiency of PMT: 20 %.
- amplification gain of PMT:  $5 \times 10^6$ .
- Rise/Fall time of single photoelectron signal: 10/15 ns.
- Specific impedance of the signal cable: 50  $\Omega$ .
- Load impedance of PMT output including a back termination: 25  $\Omega$ .
- Sampling rate of the FADC: 500 MHz.
- Input voltage range of the FADC:  $\pm 0.3$  V.
- Resolution of the FADC: 8 bits ⇒ 2.3 mV/ch.
- Amplifier gain: 10.
- Attenuator ratio: 5:1.
- Trigger threshold for one PMT: 0.25 p.e. equivalent.

#### 2. One photoelectron signal

Approximating the signal shape to a triangle with 10 ns rise time and 15 ns fall time, the peak voltage of the one photoelectron signal is 1.6 mV. After the amplifier of gain 10, it corresponds to 7 FADC counts. The signal is distributed to 13 bucket wide. The trigger discrimination is applied to the output data of digital integrator. The integrated FADC counts for one photoelectron is 44, and 0.25 p.e. PMT trigger threshold corresponds to 11 counts. In actual signals, the shape of the tail is exponential and the signal will distribute to much wider time span than 25 ns and the integration period will be 50 ns.

#### 3. Low energy signals

An average number of photoelectrons created at one PMT for 1 MeV signal is 0.45 p.e. Thus half of PMT do not have a hit and 0 suppression is effective to reduce the data size. The maximum energy for the reactor neutrino signal is 9 MeV, which produces 4.1 p.e./PMT of scintillation light if the event occurs at the center of the detector. Because events

occurred near the acrylic wall deposit 3.5 times more light to the nearest PMT than those occurred at the center of the detector, the nearest PMT will generate 14 p.e./PMT for such peripheral events with energy 9 MeV. The dynamic range of the FADC corresponds to 37.5 p.e., which safely covers the maximum reactor neutrino energy.

#### 4. High-energy signals

A penetrating cosmic muon causes as much as 750 MeV of energy deposit, because the maximum track length in the scintillators is 5 m. 750 MeV of energy deposit produces 350 p.e./PMT of scintillation light. This is out of dynamic range of the FADC system and at least 1/5 of attenuation is necessary. If the scintillation light comes at the same time, the pulse height from the PMT becomes 1.5 V. The output of the amplifier will saturate for this kind of signals and fast recovery from the saturation is required to the amplifier. A clipping diode can be installed to the amplifier input.

Another idea to treat this issue is to install smaller diameter PMTs in addition to 10" PMT, which is now our baseline scheme. If 2" PMT is used, the aperture of the PMT is 1/25 of the 10" PMT and the number of photoelectron obtained by PMT is as much smaller and the PMT will not saturate even for cosmic-ray signals. This information is used to judge the cosmic-ray is showering or not and set additional dead time for showering muons.

### 5.3 Trigger

The basic trigger is issued for events which have energy greater than 0.7 MeV. All the events with the energy greater than the threshold are recorded. For this energy the number of expected photoelectron is 0.3 p.e./PMT. Thus the energy of the signal approximately corresponds to the number of hit PMTs and the global trigger is issued based on the multiplicity of the hit PMTs. The hit multiplicity for 0.7 MeV signal is about 90 PMT hits. A PMT hit is defined by 'PMT trigger', which is issued when the 50 ns-wide integrated FADC hits becomes 0.25 p.e. level or more. The PMT hit information is also used for 0-suppression procedure. The integration of the FADC data and the summation of PMT hits are performed by field programmable gate arrays (FPGA) as shown in Fig. 45. The information of the PMT trigger from all the PMTs are sent to the global trigger module and total number of hits with integration time of 100 ns is calculated. The trigger circuit can generate more sophisticated trigger, such as delayed coincidence + low threshold trigger, pre-scaled trigger, random trigger, GPS trigger for absolute time stamp, forced trigger for calibrations, etc.

### 5.4 Readout modules

The FADC module is composed of a daughter board, which is a main part with a FADC chip, and a mother board which works mainly as an interface to the

readout bus.

1. Daughter board: It includes a buffer amplifier whose gain is selected either 10 or 1/5 by a jumper. The input impedance is selectable either high or low by a jumper, so that two FADC units can be connected by a daisy chain of one input as a high gain FADC and a low gain one. Fig. 46 shows a schematic of the input circuit of FADC module. It is also usable as independent FADC channels, as well. The amplifier is followed by a FADC chip, which is 8-bit 500 MSPS ADC as a baseline. It will be driven by a 500 MHz clock in the present design. The input voltage range is  $\pm 0.32$  V.
2. Mother board: It includes FPGAs which work as controllers of the module and an interface with rear-end electronics which will be either Compact-PCI or VME.

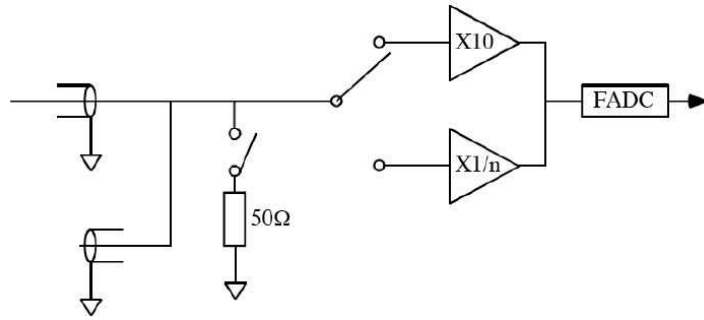


Figure 46: FADC modules input

Timing depth of one piece of data is 300 ns, which is determined by both pulse duration for the fast component and the expected latency of the trigger. The FADC chip is always active and the digitized data are written on a bank of memories in a FPGA. When the module receives a trigger from the global trigger circuit, the currently active bank and associated counter is frozen and the module activate the next bank in turn. The frozen memories are then read out to the rear-end electronics, while the next data are independently read into another bank. This feature of multi-buffer memories is adopted for deadtime-less DAQ, that is essential for the present experiment. The time interval between a buffer and a successor is measured by the absolute time stamp.[44]



## 6 Calibration

### 6.1 Introduction

Because reactor  $\theta_{13}$  measurement needs a high precision and reliability, intense calibrations are necessary throughout the run time. Calibration sources are classified into two categories. One category is optical and electronic sources, such as diffusive laser ball, optical fibers, LED and so on. The sources are used to measure responses of PMT and electronics and performs relative calibration. The other category is energy and position calibration sources. These are radioactive sources (gamma source, neutron source, positron source). Gamma sources are used for determination of absolute energy scale and energy resolution. Neutron and positron sources are used for measurements of detection efficiency and response. In addition, in order to locate a source at aimed positions, a calibration manipulator system will be developed.

	Source	Feature
Optical	Diffusive laser ball (SNO)	Isotropic laser
	UV laser (CTF-Borexino)	Pulsed laser
	LED	simple
Neutron source	$^{241}\text{Am}-^9\text{Be}$	with 4.4 MeV gamma ray
	$^{252}\text{Cf}$	spontaneous fission
Gamma source	$^{137}\text{Cs}$	0.662 MeV
	$^{54}\text{Mn}$	0.835 MeV
	$^{60}\text{Co}$	1.173, 1.333 MeV
	$^{65}\text{Zn}$	1.35 MeV
	$^{40}\text{K}$	1.5 MeV
	H neutron capture	2.22 MeV
	$^{12}\text{C}$ neutron capture	4.95 MeV
	Gd neutron capture	8 MeV
	p-T source (SNO)	19.7 MeV(Q value)
Positron source	$^{22}\text{Na}$	2.8y, 0.511 MeV, 1.275 MeV
	$^{68}\text{Ge}$	280d, alternative energies
	Michel positron	$E_{max}=53$ MeV

Table 13: various sources

### 6.2 Optical and electronic calibrations

The purpose of optical and electronic calibrations is to check the response of each PMTs and to monitor the attenuation length of liquid scintillators. An UV pulsed laser can be used for monitoring of performances such as one p.e. gain, uniformity, timing and pedestal, of each PMT. An isotropic light source like a

diffusive laser ball (SNO) can be used for monitoring the attenuation length of the detector components.

### 6.3 Energy calibration

In an antineutrino event, the positron produced by inverse- $\beta$ -decay interaction loses its energy and annihilates with electron in LS and the total energy deposit is detected as a prompt signal by the PMTs. In addition, neutron produced by the inverse-beta interaction is captured by Gd after about  $30\mu\text{sec}$ , and gamma rays are emitted that are detected as a delayed signal by the PMTs. Therefore  $\gamma$  ray source, positron source and neutron source are used for energy calibration.

#### 6.3.1 $\gamma$ ray sources

The purpose of using  $\gamma$  ray sources for calibration is to determine the absolute energy scale and energy resolution. Gamma ray sources can be classified into low energy region corresponding to the prompt signal response (0.7~9.0 MeV) and high energy region corresponding to the delayed signal response (5.0~11 MeV). There are many kinds of gamma ray sources in the low energy region. For example,  $^{137}\text{Cs}$ (0.662MeV) and  $^{60}\text{Co}$ (1.173MeV+1.333MeV) are useful sources in the low energy region. On the other hand, there are little kinds of gamma ray sources in the high energy region, because it is difficult to produce long life and high rate sources. Therefore, if we need gamma source in high energy region, one option is to develop an original source like pT source used by SNO experiment.

#### 6.3.2 Positron sources

The purpose of calibration using positron sources is measurement of positron response.  $^{22}\text{Na}$  is a very useful source because of having longer life (2.8 years) than other positron sources. Positron produced by  $\beta^+$  decay annihilates with electron in the source package, and then two gamma rays (0.511 MeV) emit back to back. In addition, one more gamma ray (1.275 MeV) emits. These annihilation gamma rays are used as mimic signals.  $^{68}\text{Ge}$  is a useful source, too, because of emitting gamma rays with alternative higher energies, but the half life is relatively short (287 days). Another way is to use cosmic rays. If  $\mu^+$  stops in the LS, it decays and produce energetic positrons in the LS.

$$\mu^+ \rightarrow e^+ + \nu_e + \bar{\nu}_\mu. \quad (17)$$

The energy distribution of this positron (Michel positron) is well known and it can be used to calibrate energy range up to 50 MeV.

### 6.3.3 Neutron sources

The purpose of calibration using neutron sources is the measurement of neutron capture response by the nuclei (H,  $^{155}\text{Gd}$ ,  $^{157}\text{Gd}$ ) in LS. Gamma rays produced by neutron capture of H,  $^{155}\text{Gd}$  and  $^{157}\text{Gd}$  give a total energy of 2.223 MeV, 8.536 MeV and 7.937 MeV respectively. Especially, the neutron capture by  $^{155}\text{Gd}$  and  $^{157}\text{Gd}$  with large cross sections is the main response of the delayed signal in KASKA experiment, and we measure absorption probability and timing by using neutron sources.  $^{241}\text{Am}$ - $^9\text{Be}$  source is useful for this purpose. In Am-Be sources,  $\alpha$  particle produced by  $^{241}\text{Am}$  decay is irradiated to  $^9\text{Be}$  nucleus, and then it forms excited state of  $^{13}\text{C}$  and decays to neutron plus 4.4 MeV  $\gamma$ .  $^{252}\text{Cf}$  is a spontaneous fission source and can produce high rate neutrons.

## 6.4 Calibration device manipulator

### Region-I

A very basic calibration equipment is a vertical string suspendable in the LS. Calibration sources are put in the known position along the  $z$ -axis. This type of calibration will be most frequently performed. In KASKA experiment, three dimensional calibration is necessary to study the properties of signals near the acrylic walls. In order to accurately locate sources at target positions, we develop a calibration manipulator. We have two candidates of manipulator types, wire type like SNO and robot arm type. For the wire type, the area of the device that shadows the scintillation photons is small. However, for the wire type, the anchors hanging the wires may damage the acrylic vessel if the load to the anchor is too strong. In addition the anchors and wires must be kept in the LS. On the other hand, by the robot arm type, all components can be taken out of the LS for physics running, and the direction of sources can be controlled. In addition, by replacing the source with a CCD camera, we can perform visual inspections, during the oil filling and to measure absolute positions of the 3 dimensional calibration device by comparing with the positions of LEDs which are distributed around acrylic sphere or PMT sphere.

### 6.4.1 Wire type manipulator

Fig.-47-left shows how to locate the calibration source in the detector by a wire type manipulator. The concept is to use a wire manipulator as in SNO detector. Four ring-blocks are attached inside the inner acrylic sphere and a wire goes through the ring. One end of the wire is tied to the calibration device and the other end goes all the way up to the top of the chimney and the length are controlled by a stepping motor. By controlling the length of the three wires, the position in the horizontal plane is determined. The 4th wire directly comes down the chimney and is attached to the top of the calibration device. The weight of the calibration device is heavier than that of LS and by controlling the length of the 4th string, the vertical position of the calibration device is defined. The basic calibration is frequently performed to put a radioactive source

along the vertical line. Then less frequently 3 dimensional calibration will be performed.

#### 6.4.2 Robot arm type manipulator

Fig.-47-right shows how to locate the calibration source in the detector by a robot arm type manipulator. By using two joints and a rotating bar going through the chimney and a connecting arm, sources can be located at target points. In addition, by using the joint connecting a source to arm, the direction of the source can be controlled. By making air chambers inside the arm, it is possible to make it zero-buoyancy to make the force to move the joint small.

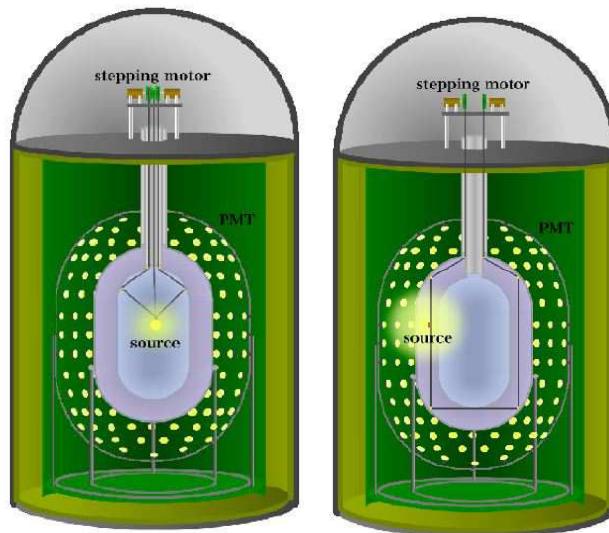


Figure 47: Source manipulator

#### Region-II

As for the Region-II, the main purpose of the calibration is to monitor the change of light output and attenuation length. String guides will be equipped in the Region-II as shown in Fig.-48. A string runs through the string guides. Radioactive sources are connected to the string and moved along the vertical direction by controlling the length of the strings.

#### Region-III

Low luminous LEDs, high luminous infrared LEDs and CCD cameras are mounted on the inner surface of the stainless steel tank. The low luminous LEDs are used to provide one photon level signals to PMTs to monitor the PMT gain easily.

High luminous LEDs are placed at known positions and become a fiducial marks for the CCD cameras. The CCD cameras are used to watch the condition of the detector and to measure the position of the calibration sources making use of LEDs as reference positions.

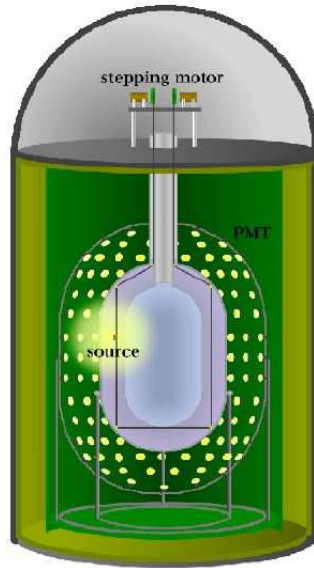


Figure 48: Region II calibration

## 7 Backgrounds

The background reduction and its precise estimation is a main issue of KASKA experiment because the uncertainty associated with background estimation is one of the most severe sources of the systematic error and the detector system has to be designed carefully to eliminate it.

Fig.49 shows an example of the background measured in CHOOZ experiment.

The events in region-D are caused by accidental coincidence of  $\gamma$ -rays from detector material and rocks. Those in Region-C are interpreted as correlated background caused by fast neutron. The events in region-A are caused by accidental coincidence between  $\gamma$ -rays and high energy signals such as recoil protons. The events in region-B can be associated with decaying muon after stopping in the detector. Those backgrounds leak in the neutrino candidate region and CHOOZ experiment observed 4.0% of correlated background and 1.7% of accidental backgrounds.

The Kashiwazaki-Kariwa nuclear power station has 7 reactors and it is im-

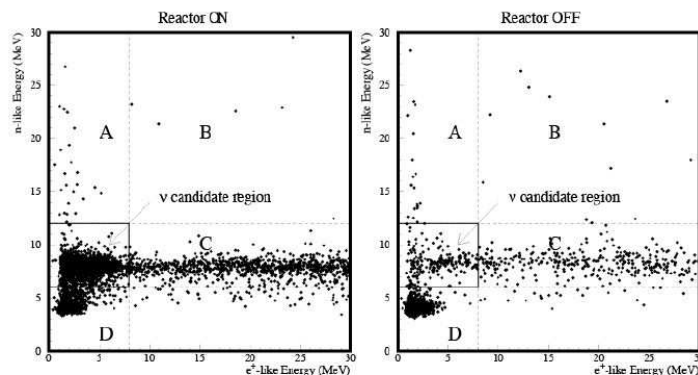


Figure 49: Correlation of prompt energy and delayed energy measured by CHOOZ group [10]. The left data were taken during reactor ON and the right data, during reactor OFF, showing backgrounds. The events in Region-A and D are caused by accidental coincidences, Region-B are caused by a Michel electrons from stopping  $\mu$  and Region-C are supposed to be caused by the fast neutron background.

possible to take reactor-off data. The strategy of the KASKA experiment for the background evaluation is to reduce the absolute background rate to be less than a few% level and then to make the absolute error of the background estimation smaller than a half %, by making use of the following methods.

(1) Powerful reactors: The Kashiwazaki-Kariwa nuclear power station is the world most powerful reactor complex whose thermal power is 24.3GW, which produces 3 times more neutrinos than CHOOZ power station. With this high neutrino flux, the S/N ratio and statistics become large at a given detector configuration.

(2) Underground laboratory: The neutrino detectors are placed in a tunnel excavated at the bottom of deep shaft holes to reduce the cosmic-ray rate. The most severe backgrounds, such as fast neutron and correlated signals from spallation products are originated by cosmic rays. The water-equivalent depth of the far detector is 260 mwe, which reduces the cosmic ray rate down to 1/240 of that on the surface. For near detectors, the depth is roughly 90 mwe which reduces the cosmic-ray rate down to  $\sim 1/30$ .

(3) Gd loaded liquid scintillator: The total energy of the  $\gamma$ -rays from the neutron captured Gd is  $\sim 8$  MeV. This is much larger than the highest natural  $\gamma$ -ray energies of 2.6 MeV and natural highest  $\beta$ -decay energy of 5 MeV. Thus the delayed signal is free from background of natural radio isotopes.

(4) Thick shields: The external backgrounds such as  $\gamma$ -rays and fast neutrons can be reduced by thick shields. Fig.-50 compares the KASKA detector and the CHOOZ detector. The thickness of the KASKA shield is much thicker than

that of CHOOZ detector and the external backgrounds are significantly reduced compared with the CHOOZ case. An option is to make the buffer oil as a weak scintillator having a light output of 1/10 of Gd-LS. 90 cm thick buffer between

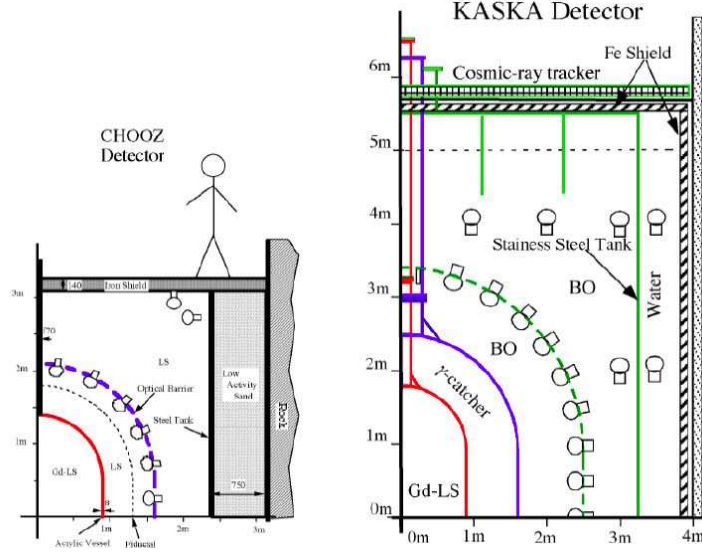


Figure 50: Comparison of the CHOOZ and KASKA detector.

PMT array and the liquid scintillator reduces the  $\gamma$ -rays from PMT glass. There is at least 2.2m thick buffer and water barriers between the liquid scintillator and iron tank. The  $\gamma$ -ray and neutron background from outside of the detector is reduced to negligible level with these buffers.

(5) Cosmic-ray tracker: When cosmic-ray hit  $^{12}\text{C}$ , radioactive elements are produced by spallation reactions. Among them, long lived  $\beta$ -neutron emitters, such as  $^9\text{Li}$  or  $^8\text{He}$  are most significant background sources. Because spallation products are produced along the cosmic-ray track, the rate of such kind of background can be estimated by the distribution of distances between the cosmic-ray track and signal candidate. A cosmic-ray tracker system is implemented to estimate this kind of spallation backgrounds.

## 7.1 Background Sources

Background signals are caused by radioactive elements such as  $^{238}\text{U}$  ( $\tau = 4.5 \times 10^9 y$ ),  $^{232}\text{Th}$  ( $\tau = 1.4 \times 10^{10} y$ ),  $^{40}\text{K}$  ( $\tau = 1.3 \times 10^9 y$ ) and  $^{60}\text{Co}$  ( $\tau = 7.6 y$ ).  $^{238}\text{U}$ ,  $^{232}\text{Th}$  and  $^{40}\text{K}$  naturally exist in various materials due to their extremely long lifetime while  $^{60}\text{Co}$  is artificially contaminated in steels in smelting process.

Fig. 51 shows the decay chain of the  $^{238}\text{U}$  and  $^{232}\text{Th}$ . If radioactive elements decay within liquid scintillator, both  $\beta$  and  $\gamma$  rays contribute as background (Internal background). The  $\alpha$  particles can not be a background because the

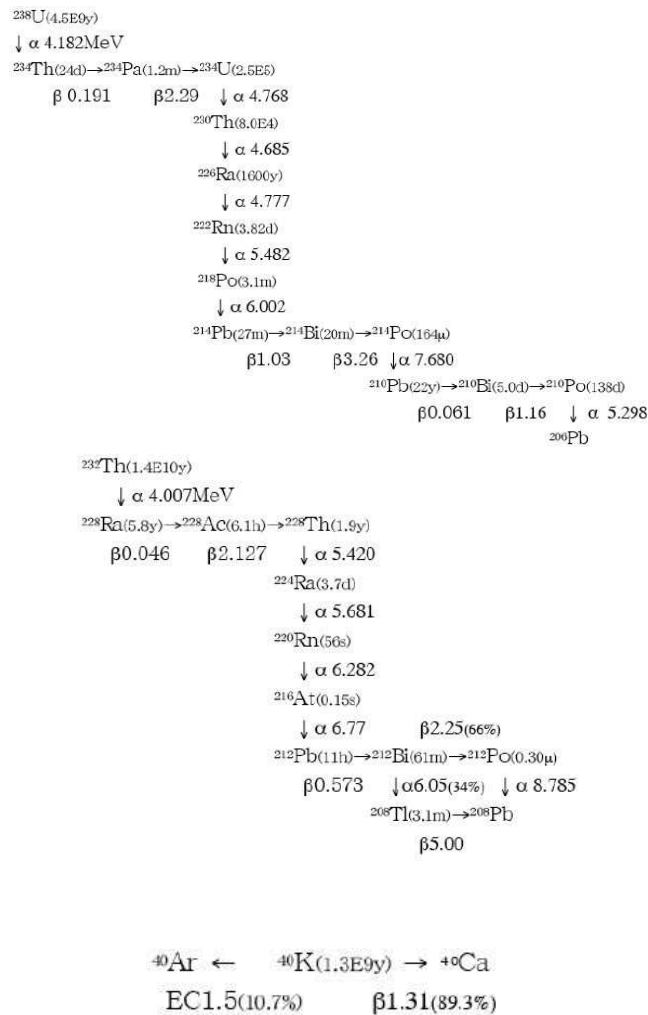


Figure 51: Decay of  $^{238}\text{U}$  chain,  $^{232}\text{Th}$  chain and  $^{40}\text{K}$ .



visible energy of the  $\alpha$ 's produced in natural radio isotopes are quenched to less than 0.5 MeV. If these elements decays outside the liquid scintillator, only  $\gamma$ -rays contribute as background since the range of a few MeV  $\beta$  is only a few cm (External background). Table 7.1 shows their background rates which satisfy the positron energy window. The highest decay energy of the  $\beta$  decay is 5 MeV ( $^{208}\text{Tl} \rightarrow ^{208}\text{Pb}$  in  $^{232}\text{Th}$  chain) and these radioactive elements do not satisfy the neutron signal criterion of  $E > 5$  MeV. The backgrounds for Gd signal are caused mainly by actual neutron absorption, where the neutrons are produced by cosmic-ray associated reaction with materials.

Table 14: U, Th, K, Co activities

Element	Bq/g	# $\gamma$ /decay (E>0.7MeV)	# $\gamma$ /g	# ( $\gamma + \beta$ )/decay (E>0.7MeV)	# ( $\gamma + \beta$ )/g
$^{238}\text{U}$	12,400	2	25,000	3	37,000
$^{232}\text{Th}$	4,100	1.5	6,200	2	8,200
$^{40}\text{K}$	255,000	0.11	28,000	0.5	130,000
$^{60}\text{Co}$	-	2	-	1	-

Table 15: Internal background

Component	Quantity (kg)	$^{238}\text{U}$ (ppt)	$^{232}\text{Th}$ (ppt)	$^{40}\text{K}$ (ppt)	$\beta + \gamma$ rate (Hz)
Scintillator Oils	25,000	< 0.1	< 0.1	< 0.1	< 0.5
PPO	150	4	< 50	4.2	< 0.17
bis-MSB	2.5	48	60	6.8	0.008
Gd	6.1	8.4	12	< 1200	< 0.96
Acrylic	700	8	50	8.2	1.2
Internal Total					< 2.9

### 7.1.1 Internal Background

\* The liquid scintillator

The amount of oil used for both LS-I and LS-II is 25 tons. The liquid scintillator will be formulated by dissolving PPO, bis-MSB and organic Gd into an oil which is made mainly of pseudocumene and paraffin oils. The U/Th/K contamination of these materials has been measured by ICP-MS and flame atomic absorption method. The oils are produced from a number of steps of distillation and refinery processes and are intrinsically pure. The U/Th/K contaminations are less than  $10^{-13}\text{g/g}$  and the total single rate from oil is less than 0.5 Hz. The single rate from PPO, bis-MSB and Gd samples were estimated to be less than

1.2 Hz from its measured contaminants.

\* Acrylic vessels

The weights of the inner and outer acrylic vessels are 240 kg and 900 kg, respectively. Because half of the  $\gamma$ -rays from the outer acrylic vessel do not come in the scintillator region, the effective mass of the outer vessel is 450 kg and the effective total acrylic weight is about 700 kg. The single rate from acrylic tanks are estimated to be 1.2 Hz.

In summary, the internal background is expected to be  $< 2.9$  Hz as shown in table 7.1.

### 7.1.2 External Background

For external background, only  $\gamma$ -rays can enter liquid scintillator.

Table 16: external background [46]

Material	Quantity (ton)	$^{238}\text{U}$ (ppb)	$^{232}\text{Th}$ (ppb)	$^{40}\text{K}$ (ppb)	$^{60}\text{Co}$ (mBq/kg)	Hit rate ( $>0.7\text{MeV}$ )(Hz)
PMT Glass	0.3	46	120	10	-	1.2
PMT support	2	1.9	4.7	0.08	9	0.2
S. S. Tank	32	1.9	4.7	0.08	9	0.05
Iron Tank	300	1.9	4.7	0.08	9	0.01
Soil	-	3,000	8,000	2,000	-	0.15
Concrete	180	2,800	5,400	1,700	-	0.43
Total						2.0

\* PMT Glass

In KASKA, 300 10" PMT will be used. The total weight of the PMT glass is 300 kg. For Hamamatsu low background glass, U/Th/ $^{40}\text{K}$  contaminations are measured to be 46 ppb, 120 ppb and 10 ppb, respectively and 650/s of  $\gamma$ -rays which satisfy the positron energy cut are generated from the glass. After penetrating 70 cm thick buffer oil, the single rate in the LS becomes 1.2 Hz.

\*  $\gamma$ -rays from the stainless steel and iron structure.

The mass of the stainless steel tank, PMT and steel tank is 30 tons, 2 tons and 300 tons, respectively. Generally a steel contains  $\sim 10\text{mBq/kg}$  of  $^{60}\text{Co}$  as well as U/Th/K.  $^{60}\text{Co}$  emits two  $\gamma$ -rays whose energies are, 1.17 MeV and 1.33 MeV. After passing through at least 90 cm of buffer oil, the single rate in the LS becomes 0.25 Hz.

\* gamma rays from soil & concrete:

The radioactive contaminations in the soil at the near-B point are measured in

a boring study to be, U/Th/K=3/8/2 ppm. A simulation shows the single rate of  $\gamma$ -ray hit from soils and concrete is only 0.6 Hz

The total single rate which is originated from natural radio activities is expected to be  $< 5$  Hz. Fig. 52 shows the simulated external background spectrum.

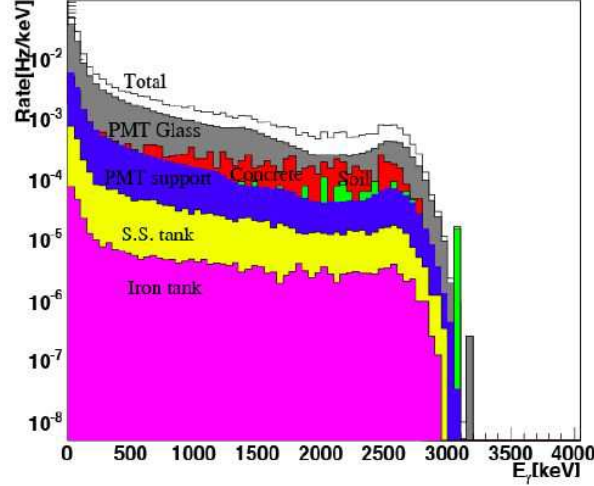


Figure 52: External background spectrum [46]

### 7.1.3 Cosmic Rays

In order to reduce cosmic-ray associated background, the detectors are placed at 150m depth underground for far detectors and at 50m depth for near detectors. The mean density of the soil around Kashiwazaki-Kariwa Nuclear Power station is  $1.75\text{g}/\text{cm}^3$ . 30 weight % is water component. The water equivalent overburden at 150 m underground is 260 meter-water-equivalent (mwe) and that at 50 m underground is 90 mwe. Fig-53 shows the cosmic ray flux at various depth calculated by an empirical formula [48];

$$I(h) = 1.4 \times \frac{1,740,000}{h + 400} \times (h + 11)^{-1.53} \exp(-7.0 \times 10^{-4}h) [\text{m}^2/\text{s}] \quad (18)$$

where  $h$  is the depth measured in mwe and the factor 1.4 is a normalization factor which is chosen to match to our simulation result at 150m depth. Fig. 54 shows the energy spectrum and zenith angle distribution at far detector depth [47]. At 150m depth, the cosmic ray flux is  $\sim 0.55/\text{m}^2/\text{s}$  and at 50m depth it is  $\sim 6.6/\text{m}^2/\text{s}$ . The cosmic-ray hit rate at inner detector region (region-I, II,

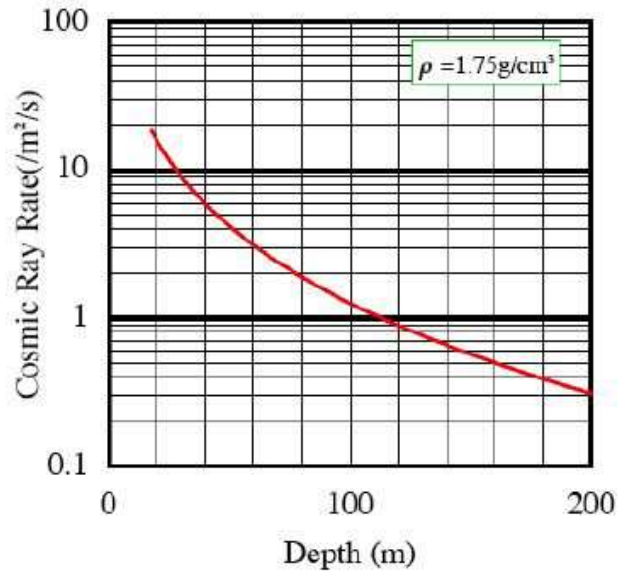


Figure 53: Cosmic Ray Rate

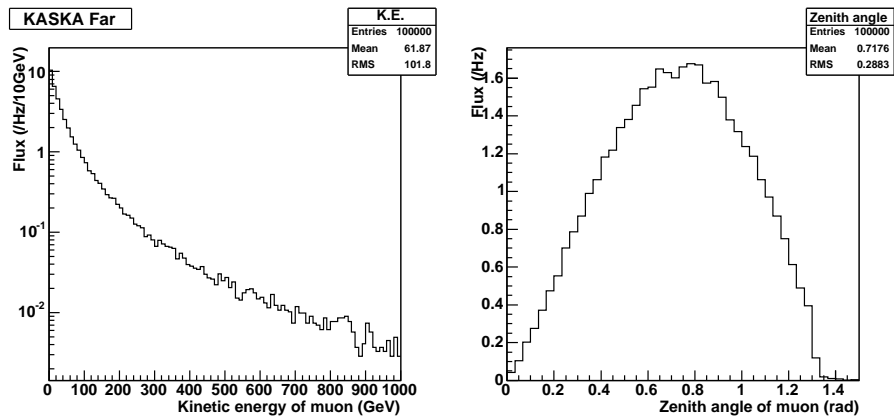
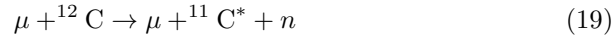


Figure 54: Cosmi ray energy spectrum (left) and zenith angle distribution (right) at far detector depth [47].

III) is  $\sim 15$  Hz for far detectors and  $\sim 170$  Hz for near detectors. The hit rate at outer detector region (region-IV, V) is  $\sim 40$  Hz for far detectors and  $\sim 500$  Hz for near detectors. The mean energies of the cosmic rays are  $\sim 70$  GeV and  $\sim 20$  GeV, respectively.

The cosmic-ray veto system consists of at least 1.6 m thick buffer oil in region-IV for vertical direction and 0.7 m thick buffer oil in region-IV and 0.5 m thick water in region-V in horizontal direction. A minimum ionizing particle deposits at least 260 MeV of energy in region-IV at vertical direction, 110 MeV of energy in region-IV and 100 MeV of energy in region-V at horizontal direction. Together with the water cherenkov veto and cosmic-ray tracker,  $>99.5\%$  of cosmic-ray rejection efficiency is expected. A fast neutron which collides with a proton in the region-IV and deposit visible energy of few MeV is also expected to be vetoed by cosmic-ray anti counter. In order to avoid the instantaneous cosmic-ray associated backgrounds, 0.5 ms of dead time will be applied after each muon passage in the liquid scintillator region and 0.2 ms of dead time is set after the muon passage in non scintillating region. The livetime inefficiency introduced by those dead time is around 1.6 % for far detectors and 20 % for near detectors. The  $\bar{\nu}_e/\mu$  rate is higher for near detectors than far detectors and the mean muon energy at near detector depth is only 1/3 for far detector depth. Therefore the N/S of cosmic-ray associated background in near detectors is a half of that of far detectors.

The liquid scintillators consist of hydrocarbonic oils and chemicals which consist of hydrogen, carbon, nitrogen and oxygen. When a cosmic ray hits such nucleus, it may break the nuclei producing radioactive nucleus. However, the atomic components of the LS's are roughly H:C:N:O=1.8 : 1 :  $O(10^{-3})$  :  $O(10^{-2})$  and carbon contributes mainly to such spallations. An example of such reaction is,



The excitation of the produced nucleus decays instantly and its signal is killed by cosmic-ray veto. However,  ${}^{11}\text{C}$  decays with electron capture with half life of 20.4 ms, which is long enough to survive the cosmic-ray veto. The neutron produced will be absorbed by proton or Gd, which produces a delayed signal. Fig. 55 shows a list of long lived radioactive elements which can be produced by spallation of carbon nucleus. Table 17 shows their production rate in region I and II, calculated by using the cross sections taken from [50] and assuming that the cross section is proportional to  $\bar{E}_\mu(\text{GeV})^{0.75}$ , where  $\bar{E}_\mu$  is a mean energy of cosmic-rays. The total production rate within region-I and II is 0.036/s for far detector and 0.27/s for near detectors, both are much smaller than  $\gamma$ -ray rate from detector materials. If the neutrons produced by the spallation reaction is absorbed by Gd, they generate delayed signal. The rate of such neutron signal which survives the cosmic-ray veto time is,

$$f_n < N_n f_I \left( \exp\left(-\frac{T_{\text{veto}}}{30\mu\text{s}}\right) + \beta \exp\left(-\frac{T_{\text{veto}}}{200\mu\text{s}}\right) \right), \quad (20)$$

n/z	0	H 1	He 2	Li 3	Be 4	B 5	C 6
0		H(99.99)				stable	sunstable
1	n 10.61m b-(0.782)	2H(0.01)	3He(1.3E-6)			(abundance)	name lifetime mode
2		3H 12.3y b-(0.019)	4He(100)				
3				6Li(7.42)	7Be 53.3d EC(0.862)	8B 0.77s EC2a(1.798)	9C 0.127s ECp2a(16.50)
4			6He 0.808s b-(3.51)	7Li(92.58)	8Be 0.067fs 2a	9B 0.85s p2a	10C 19.15s EC(3.648)
5				8Li 0.844s b-2a(1.60)	9Be(100)	10B(19.7)	11C 20.38ms EC(1.98)
6			8He 0.122s b-n(10.65)	9Li 0.178s b-n(13.61)	10Be 1.6E6y b-(0.551)	11B(80.3)	12C(98.89)
7					11Be 13.8s b-a(11.51)	12B 0.0203 b-3a(13.37)	13C(1.11)

Figure 55: Long life radio isotopes possibly produced by cosmic-ray spallation reaction of carbon [49].

Table 17: Production rate (Region-I+II)

	Far	Near
mean energy (GeV)	68	19
$\mu$ flux (/m <sup>2</sup> /s)	0.55	6.6
<sup>11</sup> C(20.4ms)	$2.6 \times 10^{-2}$	$1.9 \times 10^{-1}$
<sup>7</sup> Be(53.3d)	$5.8 \times 10^{-3}$	$4.8 \times 10^{-2}$
<sup>11</sup> Be(13.8s)	$< 5.5 \times 10^{-5}$	$< 5.0 \times 10^{-4}$
<sup>10</sup> C(19.15s)	$3.5 \times 10^{-3}$	$2.4 \times 10^{-2}$
<sup>8</sup> Li(0.844s)	$1.4 \times 10^{-4}$	$8.4 \times 10^{-4}$
<sup>6</sup> He(0.808s)	$4.6 \times 10^{-4}$	$3.3 \times 10^{-3}$
<sup>8</sup> B(0.77s)	$1.9 \times 10^{-4}$	$1.5 \times 10^{-3}$
<sup>9</sup> C(0.127s)	$1.6 \times 10^{-4}$	$7.5 \times 10^{-4}$
<sup>9</sup> Li(0.178s)+ <sup>8</sup> He(0.122s)	$6.0 \times 10^{-5}$	$2.8 \times 10^{-4}$
sum	$3.6 \times 10^{-2}$ /s	$2.7 \times 10^{-1}$ /s

where  $N_n$  is the number of neutrons produced in the spallation reaction,  $f_I$  is production rate of radioactive spallation nucleus in region-I and  $T_{\text{veto}}$  is the cosmic-ray veto time.  $\beta$  is the fraction that a neutron produced in region-II 'spills-in' to the region-I and is absorbed by Gd, which is an order of 10%. For the case of  $^{11}\text{C}$  and  $T_{\text{veto}} = 0.5$  ms,  $f_n < 3.2$  /day for far detector. For other nuclei, it is much less than that and total neutron rate is less than 5 /day.

As described in the next section, there is a case that fast neutron produced by hard collision of  $\mu$  and nucleus will be thermalized in the liquid scintillator and eventually absorbed by Gd. According to a MonteCarlo simulation, this kind of background takes place at a rate of 2.2/day in far detector assuming 99.5% efficiency for muon veto.

## 7.2 Accidental Backgrounds

Accidental background is the events in which independent background signals accidentally happens within the delayed coincidence timing window and regarded as neutrino signals.

The accidental background rate  $f_{AB}$  is expressed as,

$$f_{AB} = f_{e^+} f_n \omega \quad (21)$$

where  $f_{e^+}$  and  $f_n$  are rates of  $e^+$  like signals and neutron like signals.  $\omega$  is the coincidence window. For KASKA experiment, the energy windows for positron and neutron signals are, 0.7 MeV to 9 MeV and 5 MeV to 11 MeV, respectively. The timing window is 200  $\mu\text{s}$ .

Table 18 summarize the single rate and accidental background rate for far detector. Accidental background rate can be estimated precisely by opening coincidence window randomly.

Table 18: Single rate and accidental background summary.

Source	$f_{e^+}$ (/s)	$f_n$ (/day)
Internal	<2.9	-
External	2.0	-
Cosmic ray spallation	0.036	< 7.2
sum	< 5	< 7.2
Accidental background	<0.01/day	

For near detectors, S/N is expected to be better than far detector because the mean energy of cosmic-ray is much smaller and the reaction cross section is smaller.

## 7.3 Correlated Backgrounds

Correlated background is a signal in which a single event produces two contiguous signals, each satisfies the prompt and delayed energy windows for  $\bar{\nu}_e$  selec-

tion within coincidence time window. Fast neutron background and  $\beta$ -neutron emitting radio isotopes are categorized as correlated backgrounds.

### 7.3.1 Fast Neutron Background

When a fast neutron collides with proton in a scintillator, there is a chance that the visible energy of the recoiled proton falls in the energy window for  $\bar{\nu}_e$  prompt signals. Also there is a chance that the original neutron loses its energy scattered by protons around and eventually absorbed by Gd. In this case the fast neutron signals are misjudged as  $\bar{\nu}_e$  events. Such fast neutrons are often produced by inelastic scattering of cosmic-ray muon,

$$\mu + A \rightarrow \mu + n + X \quad (22)$$

According to the KASKA simulation, the fast neutron background (FNB) coming from the muons which go through outside of the veto system is negligibly small thanks to the thick buffer regions. Most of the FNB comes from the muons which come in the detector region but can not be detected due to the inefficiency of the veto system. For 99.5% of veto efficiency, 0.2 /day after the event selection, or  $\sim 0.7\%$  of the  $\bar{\nu}_e$  signal is expected from the simulation. The rate of FNB can be estimated by number of ways. Because most of the FNB is associated with the veto inefficiency, the rate can be estimated by applying veto inefficiency artificially when analyzing the data. It can be estimated from the energy distribution of the prompt signal in the non-reactor neutrino energies or spallation background energies, such as beyond 15 MeV and less than 1 MeV. Fig. 56 shows visible energy distributions calculated by a MonteCarlo simulation. The figure shows the energy distribution is flat down to 4 MeV and there

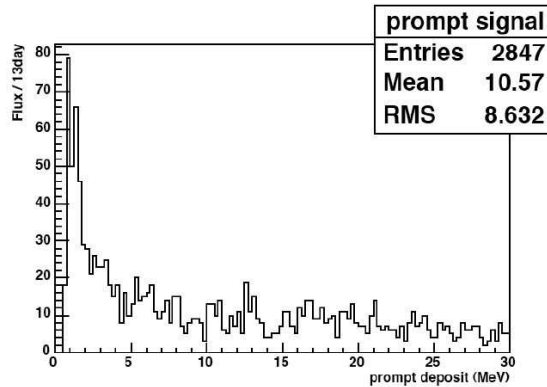


Figure 56: Visible energy distribution of delayed energy [47].

is an enhancement at  $E < 4$  MeV. The enhancement can be estimated from the event rate below 1 MeV. It will be possible to understand the energy distribution with real data by tagging cosmic-rays. The radial position dependence



of the events also gives information about fast neutron background since the neutron backgrounds tend to occur near the detector surface. The Palo-Verde type liquid scintillator and  $\gamma$  catcher liquid scintillator have neutron/ $\gamma$  pulse shape discrimination capability and this feature may be of help to separate the neutron and positron signals. Assuming the rate of fast neutron background can be estimated with  $<30\%$  accuracy, the absolute error of this background estimation is  $<0.2\%$ .

### 7.3.2 Spallation Background

Some spallation products have decay mode to produce  $\beta + n$ . In such decays, the  $\beta$  signal mimics the prompt signal of the reactor neutrino and the neutron is absorbed by Gd producing exactly same signal as reactor neutrino delayed one. Among these  $\beta + n$  emitter,  ${}^9\text{Li}$  and  ${}^8\text{He}$  are most serious background source because they can be produced from  ${}^{12}\text{C}$  and have long lifetimes and can not be rejected by the veto time applied after muon passage.

KamLAND group showed that  ${}^9\text{Li}$  dominates and contribution from  ${}^8\text{He}$  was less than  $15\%$  [51] in their data taken at 1000m deep underground and its amount is consistent with reference-[50]. According to the reference, the production rate of  ${}^9\text{Li}+{}^8\text{He}$  in region-I is 1.2 /day for far detectors. Because the branching ratio of the  $\beta - n$  decay mode is  $50\%$  for  ${}^9\text{Li}$  and  $16\%$  for  ${}^8\text{He}$ , the neutron associated background rate becomes at least half, which corresponds to  $<1.5\%$  of the reactor  $\bar{\nu}_e$  events. The other  $\beta - n$  emitters are assumed to be at least  $O(10^{-2})$  times smaller because they have to be produced from oxygen nuclei. The  ${}^9\text{Li}$  background rate can be estimated with following methods.

\*Energy Spectrum: Because the Q value for neutron associated decay of  ${}^9\text{Li}$  is 11.2 MeV, this background can be estimated from the number of events between 9 MeV to 11 MeV.  $\sim 5\%$  of  ${}^9\text{Li}$  signals falls in this non  $\bar{\nu}_e$  energy window.

\* Cosmic-ray track: Because decay mode of the  ${}^9\text{Li}$  is  $\beta$  decay, the prompt like signal occurs within a few cm along the cosmic-ray track.

The production cross section and its extrapolation on mean muon energy was measured with accuracy  $20\%$  [50]. Assuming the background rate can be estimated with precision  $<30\%$ , the absolute error comes from this background is  $<0.5\%$ .

### 7.3.3 Stopping $\mu$

Fig. 57 shows the probability for cosmic-rays to stop after passing through  $1\text{ g/cm}^2$  of material. In order for cosmic rays to satisfy visible energy criteria of prompt energy selection, the muons have to stop at less than 40 cm from the PMT layer if weak scintillator is used for the buffer oil. The probability to stop less than 40 cm in the region-III oil is  $0.4\%$  and absolute rate is  $\sim 200/\text{hr}$  for far detectors. Assuming  $99.5\%$  of cosmic-ray veto efficiency, the survival rate becomes  $\sim 1/\text{hr}$ . However, the stopping position is still in region-III and can easily be distinguished from  $\bar{\nu}_e$  events which occur within region-I.

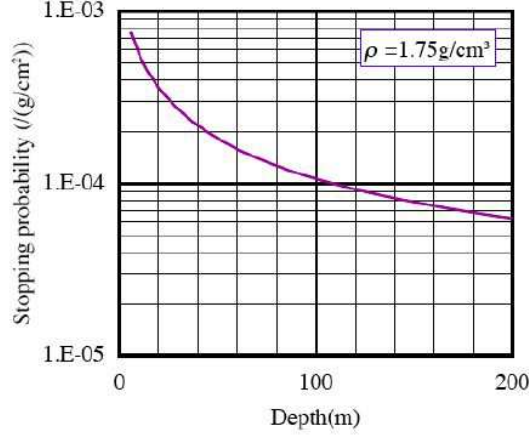


Figure 57: Cosmic-ray stopping probability.

Most of stopping muons decay as,



The maximum kinetic energy of electron or positron is 53 MeV which produce  $\sim 5$  MeV of visible energy in region-III. Some of these events satisfy the delayed signal criteria. Assuming 10% of delayed energy cut efficiency for the Michel electron, and timing cut efficiency of  $e^{-1\mu s/2.1\mu s}$ , the correlated event rate is 1.5 event/day. For  $\mu^-$  case, 7.9% of stopped  $\mu^-$  is captured on  $^{12}\text{C}$  and 80% of which goes to unstable nucleus which typically emits neutron [14],



If the stopping muon, which satisfies the prompt event selection, emits neutron, it can be a correlated background. Assuming 1 % of neutron produced by such stopping muon is captured by Gd, the rate of this background is,  $\sim 2.5$  events/day.

However, these events can be easily distinguished from  $\bar{\nu}_e$  events making use of the extreme position difference of the signals and reduced to a negligible level.

Table 19 summarizes the expected background rate and its estimation error.

For near detector case, the S/N is two times better than the far detector case and the absolute error after near/far comparison is 0.6% or better.

## 8 Systematic Error

It is difficult to accurately estimate systematic error before experiment starts. In this section an upper limit of KASKA systematic error is estimated by comparing the recorded errors by CHOOZ experiment.

Table 19: background summary

source	absolute	error
Accidental	<0.02%	negligible
Fast Neutron	0.7%	<0.2%
${}^9\text{Li}+{}^8\text{He}$	<1.5%	<0.5%
Stopping $\mu$	nagligible	negligible
Combined	<2.2%	<0.5%

### 8.1 Near/Far cancellation

If neutrino oscillation takes place, the expected neutrino spectrum;  $\mu_\nu(E)$  at distance  $L$  from a reactor is calculated as

$$\mu_\nu(E, L) = \mu_\nu^0(E, L)(1 - \sin^2 2\theta_{13} \sin^2 \Phi_{13}(E, L)) \quad (25)$$

where  $\mu_\nu^0(E, L)$  is the energy spectrum in case of no neutrino oscillation calculated by the equation below.

$$\mu_\nu^0(E, L) = \frac{1}{4\pi L^2} N_p \sigma_{\nu p}(E) f_\nu(E) \quad (26)$$

where  $N_p$  is the number of target protons,  $f_\nu(E)$  is the number of generated neutrinos in reactors and  $\sigma_{\nu p}(E)$  is the differential cross-section of the inverse neutron  $\beta$  decay,

$$\bar{\nu}_e + p \rightarrow e^+ + n \quad (27)$$

In the KASAK experiment, the oscillation will be searched for mainly by using the deficit of the total event rate. For such case, the expected number of events;  $\mu_\nu$  is,

$$\mu_\nu = \mu_\nu^0(1 - \sin^2 2\theta_{13} \Lambda(L)) \quad (28)$$

where,

$$\mu_\nu^0 = \int \mu_\nu^0(E, L) dE \quad (29)$$

is the total number of events in case of no neutrino oscillation.

$$\Lambda(L) = \frac{\int \mu_\nu^0(E, L) \sin^2 \Phi_{13}(E, L) dE}{\int \mu_\nu^0(E, L) dE} \quad (30)$$

is the deficit of event at distance  $L$  from the reactor. Fig. 58 shows  $\Lambda(L)$  for the case of  $\Delta m^2 = 2.4 \times 10^{-3} \text{eV}^2$ . At the first oscillation maximum of  $L \sim 1.8 \text{km}$ , only 20% of  $\bar{\nu}_e$  remains.

For simplicity, we assume a case to measure  $\sin^2 2\theta_{13}$  with a scheme of one reactor, and one far detector at a distance  $L$ , one near detector at a distance  $L'$ . If we observe  $N_{obs}$  events in the far detector and  $N'_{obs}$  events in the near

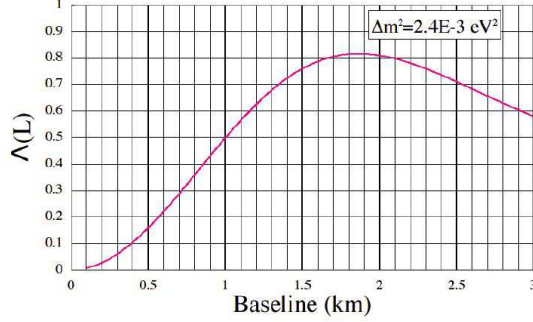


Figure 58: Deficit probability ( $\Lambda(L)$ )

detector, we consider  $\epsilon\mu_\nu = N_{obs}$  and  $\epsilon'\mu'_\nu = N'_{obs}$ , where  $\epsilon$  and  $\epsilon'$  represent detection efficiencies of far and near detectors, respectively. Therefore, the most probable  $\sin^2 2\theta_{13}$  is,

$$\sin^2 2\theta_{13} = \frac{1 - r}{\Lambda(L) - r\Lambda(L')} \quad (31)$$

where

$$r = \left(\frac{L}{L'}\right)^2 \frac{\epsilon' N'_p N_{obs}}{\epsilon N_p N'_{obs}} \quad (32)$$

is expected to unity in case of no neutrino oscillation. It is noted that  $\sigma_{\nu p}$  and  $f_\nu$  do not appear in Eq.(31) and the measurement accuracy does not directly depend on the errors on such parameters. If value of Eq.(31) is significantly larger than 0, it indicates that non-0  $\sin^2 2\theta_{13}$  is observed.

Since  $\sin^2 2\theta_{13}$  is known to be small, the measurement error is,

$$\delta \sin^2 2\theta_{13} = \frac{1}{\Delta\Lambda} \left( \sqrt{\frac{1}{N_{obs}} + \frac{1}{N'_{obs}}} + \frac{\delta_{uncorr}(\epsilon N_p)}{\epsilon N_p} + 2\frac{\delta(L/L')}{(L/L')} \right) \quad (33)$$

where  $\Delta\Lambda = \Lambda(L) - r\Lambda(L') \approx 0.7$  for KASKA base lines. In order to obtain a small error, having a large  $\Delta\Lambda$  is essential.  $\delta_{uncorr}$  means uncorrelated error for both detectors. By taking the ratio, the common uncertainty components cancel out and only uncorrelated components remain. The term of square root is the statistic error.

In the KASKA experiment, the main event selections are,

- (1)  $0.7MeV < E_{prompt} < 9MeV$
- (2)  $5MeV < E_{delay} < 11MeV$
- (3)  $1\mu s < \Delta t < 200\mu s$

The detection efficiency is multiplication of each event selection.

$$\epsilon = \epsilon_e + \epsilon_n \epsilon_{\Delta t} \quad (34)$$

Errors come in from the relative uncertainties of each parameter.

## 8.2 Detector Associated Error; $\delta_{uncorr}(\epsilon N_p)/\epsilon N_p$

### 8.2.1 Number of target protons; $N_p$

The number of target proton is calculated by,

$$N_p = M_{GdLS}\rho_p \quad (35)$$

where  $\rho_p$  is the proton density per unit LS mass and  $M_{GdLS}$  is the mass of the Gd-LS within the fiducial region. The Gd-LS for all the detectors will be stored in a storage tank before introducing in the detectors and sent to each detector from the tank. So that in principle, the component of the LS is same for all the detectors.

KASKA does not apply fiducial cut because it introduces a large uncertainty. Instead, the reactor neutrino signal is identified by existence of the neutron-captured Gd signal, regardless where the prompt signal occurs. Because region-II scintillator does not contain Gd, there is a natural cut-off of the fiducial region. The main error of the neutrino detection efficiency comes from the relative difference of the fiducial mass of the Gd-LS between the near/far detectors. The mass will not be defined by the volume of the container because it possibly deforms under the pressure of the liquids. Instead, it will be defined by total mass of the LS which is measured precisely when filled in the detector. The Gd-LS will be delivered by 200 liter oil drums and the weight difference before and after the filling is measured with 0.3% accuracy weighing machine. The three weighing machines used in the far and near detectors are cross calibrated occasionally during the filling process. The diameter of the chimney is 30 cm and 0.1% of volume error corresponds to 10 cm of head level difference, which can easily be detectable by a level monitor.

If the neutron produced in a  $\bar{\nu}_e$  event goes out from region-I, it introduces an inefficiency (spill-out effect). Contrarily even if a  $\bar{\nu}_e$  event occurs in region-II, it is considered to be  $\bar{\nu}_e$  signal if the produced neutron comes in the region-I and is absorbed by Gd (spill-in effect). The spill-in effect largely cancels the spill-out inefficiency. Fig.-59 depicts such effects. The error introduced due to the edge effects is

$$\frac{\Delta N_p}{N_p} \sim \frac{3(\Delta\sigma_I - (\rho_{II}/\rho_I)\Delta\sigma_{II})}{2R}, \quad (36)$$

where  $\sigma_I, \sigma_{II}$  and  $\rho_I, \rho_{II}$  are diffusion length of neutrons and proton density in region-I and II, respectively.  $R$  is average radius of region-I. The main error component comes from uncorrelated uncertainty of the diffusion length. Because diffusion length is insensitive to liquid scintillator components, the error is assumed to be negligibly small.

In summary the relative uncertainty of the fiducial mass is safely claimed to be better than 0.5%.

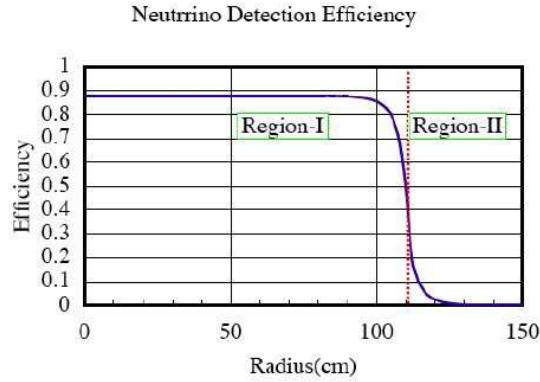


Figure 59: Radial dependence of detection efficiency. Average radius of 1.1 m is used as a typical size. Diffusion length of neutron is assumed to be 6 cm.

### 8.2.2 $e^+$ Energy Cut Efficiency; $\epsilon_{e^+}$

The threshold for the positron energy is 0.7 MeV which is  $3\sigma$  below the positron annihilation energy of 1.022 MeV. Fig. 60 shows the reactor neutrino spectrum near the energy threshold. Even if the energy resolution is  $\sigma_E/E = 15\%$  the rate below 0.7 MeV is less than 0.03% and even if 0.1 MeV of detector-relative systematic bias takes place, the relative difference in the number of event is less than 0.1%.

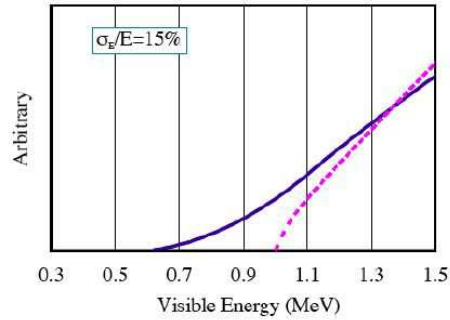


Figure 60: Energy spectra near the threshold. The dashed line shows original energy spectrum and the solid like shows the spectrum smeared by finite energy resolution of  $\sigma_E/E = 15\%$ .

### 8.2.3 Neutron Capture Efficiency; $\epsilon_n$

The efficiency for neutron signal cut is a multiply of neutron absorption efficiency on Gd;  $\epsilon_{abs}$  and the detection efficiency of Gd  $\gamma$  signal;  $\epsilon_{Gd\gamma}$ ,

$$\epsilon_n = \epsilon_{abs}\epsilon_{Gd\gamma}. \quad (37)$$

The neutron capture efficiency for Gd is expressed as,

$$\epsilon_{Gd} = \frac{1}{1 + \frac{\rho_H}{\rho_{Gd}} \frac{\sigma_H^n}{\sigma_{Gd}^n}} \quad (38)$$

where  $\rho$  is the number density of the corresponding element.  $\sigma^n$  is the neutron absorption cross section as shown in the table 20.

The ratio of the absorption cross section is  $\sigma_{abs}^p/\sigma_{abs}^{Gd} = 6.82 \times 10^{-6}$ .

Table 20: neutron absorption cross section

Element	Q value (MeV)	Abundance(%)	cross section (b)
$^1H$	2.2	99.985	$0.3326 \pm 0.0007$
$^{155}Gd$	8	$14.80 \pm 0.05$	$60900 \pm 500$
$^{157}Gd$	8	$15.65 \pm 0.03$	$254000 \pm 800$
<i>Gd Average</i>			$48800 \pm 400$

The atomic component of the KASKA liquid scintillator is

$$\#H:\#C:\#O:\#Gd=1.85:1:0.018:0.00009$$

and  $\rho_{abs}^p/\rho_{abs}^{Gd} = 2.01 \times 10^4$ . Therefore, the neutron absorption cross section on Gd is,  $\epsilon_{Gd} = 0.88$ . The capture efficiency error associated with the Gd concentration error is,

$$\frac{\delta\epsilon_{Gd}}{\epsilon_{Gd}} = (1 - \epsilon_{Gd}) \frac{\Delta\rho_{Gd}}{\rho_{Gd}} = 0.12 \frac{\Delta\rho_{Gd}}{\rho_{Gd}} \quad (39)$$

Therefore the capture efficiency is insensitive to the change of the component of the liquid scintillator. Because the Gd-LS for all detectors is taken from the same storage tank, the variation of the component is supposed to be small and the error on  $\epsilon_{Gd}$  is estimated to be better than 0.5%.

### 8.2.4 n Energy Cut Efficiency; $\epsilon_n$

The total energy of the gamma rays from neutron captured Gd is 8 MeV. The energy threshold for the neutron signal is 5 MeV, which is low enough and the uncertainty of the threshold does not cause error of the event selection. Fig. 61 shows the Gd-captured neutron signal observed by the CHOOZ group [10].

CHOOZ group assigned 0.4% as absolute error with energy threshold 6 MeV. Because the energy threshold can be set lower than CHOOZ case, thanks to a

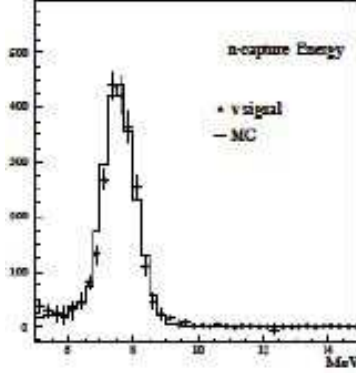


Figure 61: Gd-captured neutron signal observed by the CHOOZ experiment [10]

new buffer layer in front of PMT array, and energy containment is better, and because error of KASKA is relative error, it is expected to be much better than 0.4%. The threshold energy can be calibrated by  $n + {}^{12}\text{C} \rightarrow {}^{13}\text{C} + \gamma(5\text{MeV})$  events.

### 8.2.5 Efficiency for the timing cut; $\epsilon_{\Delta t}$

The efficiency for the timing cut is,

$$\epsilon_{\Delta t} = \frac{1}{\tau} \int_{t_1}^{t_2} e^{-\frac{t}{\tau}} dt = e^{-\frac{t_1}{\tau}} - e^{-\frac{t_2}{\tau}} \quad (40)$$

and its error is,

$$\frac{\delta\epsilon}{\epsilon} = \frac{1}{e^{-\frac{t_1}{\tau}} - e^{-\frac{t_2}{\tau}}} \left( \frac{t_1 e^{-\frac{t_1}{\tau}} - t_2 e^{-\frac{t_2}{\tau}}}{\tau} \frac{\Delta\tau}{\tau} - e^{-\frac{t_1}{\tau}} \frac{\Delta t_1}{\tau} + e^{-\frac{t_2}{\tau}} \frac{\Delta t_2}{\tau} \right) \quad (41)$$

For KASKA,  $\tau \approx 30\mu\text{s}$ ,  $t_1 = 1\mu\text{s}$  and  $t_2 = 200\mu\text{sec}$ . So that,

$$\epsilon_{\Delta t} = 0.966 \quad (42)$$

and

$$\frac{\delta\epsilon}{\epsilon} = 0.058 \frac{\Delta\tau}{\tau} - 1.0 \frac{\Delta t_1}{\tau} + 0.0014 \frac{\Delta t_2}{\tau} \quad (43)$$

The absolute timing will be quantized in unit of system clock frequency such as  $O(10\text{ns})$  and the timing of scintillation signal is  $O(10\text{ns})$ . Therefore the error induced by absolute timing is negligibly small,  $O(0.03\%)$ . Because the components of the Gd-LS is same for all the detectors, essentially  $\Delta\tau$  is small. The absorption time  $\tau$  can be measured *in-situ* with real data with precision of a few % and the  $\Delta\tau$  term is order of 0.1%.



### 8.3 Error from Reactor Neutrino Flux; $f_\nu$

The reactor neutrino flux;  $f_\nu$  is known to accuracy of 3.4%. For one reactor and 2 detectors case, the uncertainty completely cancels. However, for KASKA case, there are 7 reactors and three detector locations whose near/far baseline ratios are different. In this case the cancellation becomes imperfect and some ambiguity remains. This effect is estimated analytically in ref. [52]. The following is an intuitive description. The neutrino flux is calculated as,

$$f_\nu \sim P_{th} \times n_f \times \eta_\nu \quad (44)$$

where  $P_{th}$  is the reactor power,  $n_f$  is the fission rate per thermal power and  $\eta_\nu$  is the neutrino flux per fission. Their uncertainties are, 2%, 1%, and 2.5% respectively. However,  $\eta_\nu$  is common to all reactors and cancel out by near/far comparison. All the reactors in Kashiwazaki-Kariwa nuclear power station will be more than 10 years old and their fuel components have become equilibrium. Thus the ratio of the fission rate of each fissile element are similar when averaged over a few years of run period. Although the original error is  $n_f \sim 1\%$ , it will be canceled out to the level of negligibly small. The ambiguity from the baseline difference comes from the error of thermal power measurement, multiplied by the standard deviation of the square of the ratio of far/near baselines,

$$\frac{\delta\mu}{\mu} \sim \frac{\delta P}{P} \sqrt{\frac{1}{7} \sum_r \left(1 - \frac{R_r}{\hat{R}}\right)^2} \quad (45)$$

where  $R_r$  is the square of the ratio of far and near baselines,  $R_r = (L_r/L'_r)^2$  and  $\hat{R}$  is the average of  $R_r$ ;

$$\hat{R} = \frac{1}{7} \sum_r R_r \quad (46)$$

For KASKA case, the value of the square root in Eq.(45)  $\sim 0.07$  and the error introduced from the neutrino flux uncertainty is estimated to be 0.14%.

### 8.4 systematics summary

Since the current upper limit of  $\sin^2 2\theta_{13}$  was measured by CHOOZ experiment and the types of systematic uncertainties of KASKA experiment are similar to those of CHOOZ, it is appropriate to compare systematic uncertainties of both experiment to see the improvement of the sensitivity. Table 21 and 22 compares the systematic errors so far discussed. The total systematic error can be controlled to be better than 1% and possibly be as low as 0.5%. The  $\sin^2 2\theta_{13}$  sensitivity shown in Fig.-22 are calculated with these estimations.

## 9 Conclusions

The KASKA project enjoys world's most intense low energy  $\bar{\nu}_e$  flux from Kashiwazaki-Kariwa nuclear power station and has opportunity to pin down several neutrino

Table 21: Detector Associated Systematics Errors.

source	CHOOZ	KASKA
$e^+$ energy ( $\epsilon_{e^+}$ )	0.8%	<0.1%
$e^+$ position	0.1%	–
$n$ capture ( $\epsilon_{abs}$ )	1.0%	<0.5%
$n$ energy ( $\epsilon_{Gd\gamma}$ )	0.4%	<0.4%
$n$ position	0.4%	–
$n$ delay ( $\epsilon_{\Delta t}$ )	0.4%	<0.1%
$e^+ - n$ distance	0.3%	–
$n$ multiplicity	0.5%	–
$N_p$	0.8%	<0.5%
Combined	1.76%	<0.8%

Table 22: Systematics Summary

source	CHOOZ	KASKA
$\sigma_{\nu p}$	1.9%	negligible
Detection efficiency ( $\epsilon$ )	1.76%	<0.8%
Reactor Power ( $P_{th}$ )	0.7%	0.2%
Energy released per fission	0.6%	negligible
Background	0%	<0.6%
Combined	2.7%	<1.0%

oscillation parameters, such as  $\theta_{13}$ , precise  $\theta_{12}$  and  $\Delta m_{13}^2$ . Moreover, by combining with accelerator-based neutrino oscillation measurements, there are possibilities to find non-0  $\sin \delta$  and to solve  $\theta_{23}$  degeneracy.

The first phase of the project is to measure  $\sin^2 \theta_{13}$  with sensitivity ten times better than the current limit. The detector R&D has progressed well and it will be possible to start data taking 3 years after start of construction.

## A Acknowledgement

KASKA R&D activities have been supported by Grants-in-Aid for Scientific Research of Japanese Ministry of Education, Culture, Sports, Science and Technology and Collaborative Development Research Program of KEK. The mechanical engineering center of KEK helps development of detector structure. The KASKA group greatly appreciates them.

## References

- [1] Z.Maki, M.Nakagawa, S.Sakata, Prog. Theor. Phys. 28, 820 (1962).
- [2] Y. Fukuda *et al.* [Super-Kamiokande Collaboration], Phys. Rev. Lett. **81**, 1562 (1998) [arXiv:hep-ex/9807003].
- [3] Y. Ashie *et al.* [Super-Kamiokande Collaboration], Phys. Rev. Lett. **93**, 101801 (2004) [arXiv:hep-ex/0404034].
- [4] E. Aliu *et al.* [K2K Collaboration], Phys. Rev. Lett. **94**, 081802 (2005) [arXiv:hep-ex/0411038].
- [5] See, e.g., J.N. Bahcall, R. Davis, Jr., P. Parker, A. Smirnov, R. Ulrich eds., *SOLAR NEUTRINOS: the first thirty years* Reading, Mass., Addison-Wesley, 1994 and references therein.
- [6] Q. R. Ahmad *et al.* [SNO Collaboration], Phys. Rev. Lett. **87**, 071301 (2001) [arXiv:nucl-ex/0106015].
- [7] S. Fukuda *et al.* [Super-Kamiokande Collaboration], Phys. Rev. Lett. **86**, 5651 (2001) [arXiv:hep-ex/0103032].
- [8] K. Eguchi *et al.* [KamLAND Collaboration], Phys. Rev. Lett. **90**, 021802 (2003) [arXiv:hep-ex/0212021].
- [9] T. Araki *et al.* [KamLAND Collaboration], Phys. Rev. Lett. **94**, 081801 (2005) [arXiv:hep-ex/0406035].
- [10] M. Apollonio *et al.* [CHOOZ Collaboration], Phys. Lett. B **466**, 415 (1999) [arXiv:hep-ex/9907037]; Eur. Phys. J. C **27**, 331 (2003) [arXiv:hep-ex/0301017].

- [11] F. Boehm *et al.*, Phys. Rev. D **62**, 072002 (2000) [arXiv:hep-ex/0003022].
- [12] Y.Kozlov, L.Mikaekyan and V.Sinev, arXiv:hep-ph/0109277.
- [13] The MINOS Collaboration, P. Adamson et al., MINOS Detectors Technical Design Report, Version 1.0, NuMI-L-337, October 1998 [<http://www.numi.fnal.gov/Minos>].
- [14] K. Anderson *et al.*, arXiv:hep-ex/0402041.
- [15] Y. Itow *et al.*, arXiv:hep-ex/0106019.
- [16] Courtesy of Dr. T. Kobayashi. Similar figure is in J.Phys. G, 29, 1493 (2003).
- [17] G. L. Fogli and E. Lisi, Phys. Rev. D **54**, 3667 (1996) [arXiv:hep-ph/9604415].
- [18] H. Minakata, H. Sugiyama, O. Yasuda, K. Inoue and F. Suekane, Phys. Rev. D **68**, 033017 (2003) [Erratum-ibid. D **70**, 059901 (2004)] [arXiv:hep-ph/0211111].
- [19] P. Huber, M. Lindner, M. Rolinec, T. Schwetz, W. Winter Nucl. Phys. Proc. Suppl.145:190-193,2005 , [ArXiv: hep-ph/0412133]
- [20] <http://www.tepco.co.jp/kk-np/report2000>
- [21] [http://www.tepco.co.jp/cc/pressroom/pict\\_nu-j.html](http://www.tepco.co.jp/cc/pressroom/pict_nu-j.html)
- [22] International Nuclear Safety Center', <http://www.insc.anl.gov/>
- [23] 235U : K. Schreckenbach et al., Phys. Lett. B 160, 325 (1985),  
239,241Pu : A. A. Hahn et al., Phys. Lett. B 218, 365 (1989),  
238U : P. Vogel et al., Phys. Rev. C 24, 1543 (1981).
- [24] O.E.Mogensen, 'Positron Annihilation in Chemistry', Chemical Physics 58, Springer-Verlag.
- [25] P. Vogel and J. F. Beacom, Phys. Rev. D 60, 053003 (1999).
- [26] P. Vogel and J. Engel, Phys. Rev. D 39, 3378(1989).
- [27] Nucl. Instrum. Meth. A432, 392, 1999.
- [28] B. Achkar, et al., Nucl.Phys.B 434 (1995) 503-532.
- [29] G.Zacek, et al., Phys. Rev. D, 34 (1986) 2621.
- [30] D. N. Spergel *et al.*, arXiv:astro-ph/0603449.
- [31] V. M. Lobashev *et al.*, Nucl. Phys. Proc. Suppl. **91**, 280 (2001). C. Kraus *et al.*, Eur. Phys. J. C **40**, 447 (2005) [arXiv:hep-ex/0412056].

- [32] See e.g., H. Sugiyama, in *The Fourth International Workshop on Neutrino Oscillations and Their Origin* (NOON2003, Kanazawa, Japan), ed. by Y. Suzuki et al., World Scientific, p.300, [arXiv:hep-ph/0307311].
- [33] H.Minakata et al., Phys.Rev.D71:013005,2005.
- [34] H.Minakata and H.Sugiyama, Phys. Lett. B**580**, 216(2004), [arXiv: hep-ph/0309323].
- [35] Saint-Gobain Crystals, [www.detectors.saint-gobain.com](http://www.detectors.saint-gobain.com)
- [36] BC521 data sheet.
- [37] A.G.Piepket al., Nucl. Instr. Meth. A432, 392-398 (1999).
- [38] Anna Pla-Dalmau, Alan D. Bross, and Kerry L. Mellott. *Nucl. Instrum. Meth.* A466 (2001) 482-491.
- [39] <http://www.hpk.co.jp/Eng/main.htm>
- [40] Measurement by Prof. Y. Ooura, Tokyo Metropolitan University.
- [41] Measurement by Prof. A.Piepket, University of Alabama.
- [42] K. Nitta et al., *Nucl. Instrum. Meth.* A535 (2004) 147-151.
- [43] The Review of Particle Physics: S. Eidelman *et al.*, Phys. Lett. **B592**(2004)1
- [44] A 100MHz FADC system based on CompactPCI for DCBA.: Y. Kato, *et al.*, Nucl. Instr. & Methods. **A498**(2003)430-442
- [45] <http://www.jaea.go.jp/04/tono/index.htm>
- [46] H.Furuta, Master Thesis, Tokyo Institute of Technology (2005).
- [47] K.Sakuma, Master Thesis, Tokyo Metropolitan (2005).
- [48] 'Chronological Scientific Tables', National Astronomical Observatory of Japan.
- [49] Tables of Isotopes, 8th edition, R.B.Firestone et al., Wiley Interscience. (1996)
- [50] T. Hagner et al., Astropart. Phys. 14 33 (2000).
- [51] I.Shimizu, PhD thesis, Tohoku University (2004).
- [52] H. Sugiyama, O. Yasuda, F. Suekane and G. A. Horton-Smith, Phys. Rev. D **73**, 053008 (2006) [arXiv:hep-ph/0409109].
- [53] <http://www-numi.fnal.gov/talks/results06.html>